Spatio-temporal 1D gas–liquid model for biological methanation in lab scale and industrial bubble column

[margin annotation: multiphase reactor like the TBR]

Vincent Ngu, Jérôme Morchain, Arnaud Cockx *

TBI, Université de Toulouse, CNRS, INRAE, INSA, Toulouse, France

HIGHLIGHTS

- A dynamic multiple-way coupled 1D model for biological methanation is developed.
- H_2 and CO_2 mass transfer fluxes are accurately predicted at various scales.
- Novel bioreaction closure model relying upon physical supply and biological demand.
- The model allows predictive 1D simulation of industrial-scale bioprocess performances.

GRAPHICAL ABSTRACT

A comprehensive 1D multiple-way coupled gas–liquid model for the scale-up of biological methanation process in bubble column reactor. Industrial scale reactor image taken from www.electrochaea.com.
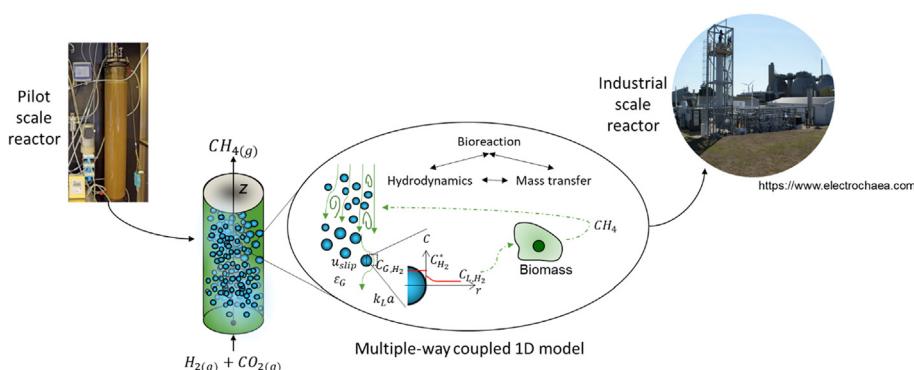
[margin annotation: modèle qui simule la façon dont différents gaz et liquides intéragissent dans un reacteur dans une seule dimension]

ABSTRACT

Numerical simulation of biological methanation in bubble column reactors is challenging due to strong coupling between hydrodynamics, mass transfer and bioreaction. A satisfactory prediction of the mass transfer coefficient and the gas solubility is crucial to couple hydrodynamics and biokinetics. A comprehensive 1D multispecies multiple-way coupled gas–liquid model is developed. The hydrodynamics of the model is validated using experimental gas loading data at very low gas holdup. The local mass transfer is validated using literature data on CO_2 mass transfer in the large-scale. The local gas holdup and interfacial CO_2 mass transfer flux are correctly described thanks to a two-way coupling between hydrodynamics and mass transfer, including changes in bubble diameter and pressure effects. When a mixture of H_2, CO_2 and CH_4 is used, highly non-linear mass transfer profiles due to differences in solubilities are observed. An original flux-based metabolic model is proposed to simulate an industrial biological methanation process. This allows smooth transition between biologically and physically controlled regimes as the culture reaches a steady-state. The comprehensive model enlightens that the biological methanation performances are governed by the H_2 mass transfer limitation balanced by growth in the transient state and biological maintenance in the steady-state.

© 2022 Elsevier Ltd. All rights reserved.

[margin annotation: When we change the process or variables and the system has not yet reached a steady state]

* Corresponding author.
  E-mail addresses: ngu@insa-toulouse.fr (V. Ngu), morchain@insa-toulouse.fr (J. Morchain), cockx@insa-toulouse.fr (A. Cockx).

1. Introduction

In the last decades, the implementation of renewable energy such as wind and solar energy has been increased worldwide, primarily due to a decline in production costs and an increasing global warming threat. However, solar and wind energy are both intermittent with unpredictable power production. In order to maintain an equilibrium between the fluctuating power production and the power demand, the presence of an energy buffer is much needed. Biological methanation emerges as an interesting solution as the surplus electricity can be stored in the form of biomethane (CH_4) through the process commonly called as "Power-to-Gas". Compared to catalytic methanation, biological methanation operates at milder condition, hence a lower investment and operation cost. A synergy effect of biological methanation with anaerobic digestor can also be established to upgrade carbon dioxide (CO_2) in the biogas to CH_4. Despite biological methanation advantages, the overall process is strongly limited by hydrogen (H_2) mass transfer (Lecker et al., 2017; Bassani et al., 2016; Rusmanis et al., 2019).

Investigation of local mass transfer phenomena in biological methanation through in silico approach is challenging especially in full scale bubble column. The hydrostatic pressure effect on the mass transfer in such tall column has to be taken into consideration. In biological methanation where the origin of the substrates and the final product CH_4 are in gas phase, a multispecies mass transfer approach has to be considered too. The strong coupling of hydrodynamics, mass transfer and reaction is evidenced through experimental findings. Giovannettone et al. carried out gas holdup measurement in a 24 m high bubble column at different liquid height. The gas holdup was found to increase with column height regardless of the sparger type or initial liquid height; with taller columns exhibiting a larger difference in gas holdup between the top and the bottom than that in shorter columns. The out of date assumption of constant gas holdup throughout the column, caused large errors in performance prediction during scale-up to industrial-scales (Giovannettone et al., 2009). In such large-scale reactors, the gaseous phase may actually undergo continuous and drastic changes in volume. As pointed out by (Di Giuliano and Pellegrino, 2019), assuming a constant superficial velocity in a 1D axial dispersion model is equivalent to imposing a constant gas holdup. Neither the case with high mass transfer rate nor the situation with volume expansion and contraction due to rapid mass transfer/reaction could valid this assumption. (Deckwer et al., 1978) conducted absorption and desorption of CO_2 in water using tall columns (4.4 m and 7.2 m high) and observed that, due to high CO_2 mass transfer rate, the gas holdup varies considerably from the bottom to the top of the column. For multispecies mass transfer, which is the most common case in industrial reactor, when one species has a higher solubility than the others, the mass transfer leads to a decrease in bubble size (Hlawitschka et al., 2017); in return, it offers a higher interfacial area for other species mass transfer. The strong coupling resides in that any changes in bubble size will influence the overall hydrodynamics behavior, resulting in a completely different slip velocity, residence time and gas fraction. In the very case of bioreactions, the spatial dependence of interfacial area and partial pressure impacts the ratio of interfacial mass transfer fluxes which determine the local availability of nutrients. These heterogeneities may induce undesired metabolic behavior as reported in many industrial bioreactor applications (Morchain et al., 2014; Pigou and Morchain, 2015).

In short, the reaction rate of biological methanation depends on the local availability of the dissolved substrates which is controlled by the gas–liquid mass transfer process and the mixing. The inter-phase mass transfer flux depends on (1) the local prevailing hydrodynamics which are controlled by the gas and liquid motion and (2) the spatially-dependent consumption by the biomass. This complex coupling of different phenomena makes the overall reactor performance prediction and scale-up of bubble column very difficult (Darmana et al., 2007). Therefore, a two-way coupling approach needs to be considered when one tries to model such strongly coupled phenomena.

The two-way coupled hydrodynamic-mass transfer problem was already addressed in the literature (Darmana et al., 2007; Nauha and Alopaeus, 2015; Inkeri et al., 2018; de Medeiros et al., 2020). Nauha and Alopaeus (2015) considered the changes in gas holdup and gas density in their compartmental model to simulate a stirred-tank bioreactor. Without including these changes, the correct interfacial area and mass transfer flux could not be estimated, leading to bad prediction of reactor performances. In Chen et al.'s works, dedicated to the simulation of synthesis gas fermentation using a 1D bubble column model, the gas holdup changes was not considered in (Chen et al., 2018, 2016, 2015). The gas–liquid mass transfer coefficients, bubble diameter, gas velocity, and gas and liquid volume fractions were treated as constants. But in a later paper of the same research group, the model included hydrodynamic spatial variation by introducing the drift-flux model (Li et al., 2019). The drift-flux model is solved according to local bubble diameter in order to obtain the local gas holdup. Inkeri et al. applied a semi-fundamental approach for the coupling of hydrodynamics and mass transfer to simulate a stirred-tank bioreactor (Inkeri et al., 2018) and a bubble column reactor (Inkeri and Tynjälä, 2020). In both studies, the local gas holdup is estimated from literature correlation through local dependent superficial gas velocity. Much like Inkeri et al. de Medeiros et al. (2020) mentioned that their 1D model accounts for the variation of gas velocity. The gas holdup is not solved, but rather estimated using literature correlation involving superficial gas velocity. Nonetheless, the results of this coupling on local concentration profile and reactor performance are not shown in their work, as it is not the objective of the paper. More recently, Hissanaga et al. (2020) developed a 1D spatio-temporal model to describe CO_2 absorption. In their work, only CO_2 is considered for mass transfer whilst the others (oxygen and nitrogen gas) behave as inert species. To our best knowledge, the two-way coupling is either empirical (through literature correlation and not-fully resolved) or its effect has not been thoroughly discussed in a 1D model framework.

Furthermore, the difficulties in modeling any biological reaction lie in the formulation of the reaction term addressing the mixing, mass transfer and bioreaction. Chen et al. (2018) developed a 1D model to simulate bioreaction using flux balance analysis. The flux balance model is a complex model which involve linear programming problem through hierarchical fixed-priority preemptive (lexicographic) optimization procedure (Chen et al., 2016). In their work on synthesis gas fermentation reactor, Siebler et al. (2020), inspired by (Linkès, 2012), proposed to compute liquid-cell mass transfer as the steady-state solution of a continuity of fluxes equation involving a Monod expression for uptake law and mass transfer diffusion limitation in the liquid phase. In the context of biological methanation, Inkeri et al. (2018) employed unstructured kinetics model, originally introduced by Schill et al. (1999) to model the bioreaction. However, they introduce an artificial stabilizing function in their model to avoid numerical issues when the substrates concentration approaches zero. Recently, Markthaler et al. (2020) used a second order kinetic law, rather than a Monod law, to model biological methanation process.

As the reaction rate of biological methanation is limited by H_2 gas–liquid mass transfer, the detailed reaction mechanism

becomes less important (Markthaler et al., 2020). In fact, the correct modeling of methanogens growth and methane production depends mainly on satisfactory prediction of the mass transfer coefficient (k_La) and the gas solubility (C^*) (Schill et al., 1999). A more practical and realistic model for biological methanation with the possibility to switch between biological regime and physical regime is therefore necessary. In this work, a comprehensive 1D spatio-temporal model considering multispecies mass transfer (H_2, CO_2, CH_4), variable gas volume fraction due to local pressure changes and mass transfer flux applied to biological methanation process is developed. The first originality is to perform a predictive resolution of partial mass balance coupled through two-phase hydrodynamics and multi-species mass transfer. The second originality lies in the formulation of the hydrogen consumption rate handling the transition from biological to physical regimes. In continuation of previous works, a universal approach to model substrate uptake rate, including gas–liquid mass transfer rate limitation is implemented (Pigou, 2018).

In a first step, the model is validated in terms of transient hydrodynamics (using experimentally measured gas holdup) and spatial mass transfer flux (using literature data). In a second step, after checking local gas liquid mass transfer fluxes for each species and global mass balances, the influences of operating pressure and reactor's height on the mass transfer and the effect of multispecies mass transfer are discussed. Lastly, an industrial-scale biological methanation plant is simulated using the proposed bioreaction expression. A step by step thorough validation of the numerical code is presented through a series of test cases along with a comparison to some experimental data when available. The goal of this model is to discuss scale-up issues as faced in the industry when multispecies mass transfer is coupled with bioreaction.

2. Material and methods

This section is dedicated to present the mathematical model and the experimental setup. The set of equations solved with the closure equations and the resolution strategy are described in Sections 2.1 and 2.2 respectively. The experimental setup and measurements are depicted in Section 2.3.

2.1. Model structure

2.1.1. General equations

The conservation of mass for the species, $i = [H_2, CO_2, etc]$ in an elementary volume of height dz takes the following form

$$\frac{\partial \phi_{G,i}}{\partial t} + \frac{\partial u_G \phi_{G,i}}{\partial z} = D_G \frac{\partial}{\partial z}\left(\varepsilon_G \frac{\partial C_{G,i}}{\partial z}\right) - k_{L,i}a(C_i^* - C_{L,i}) \tag{1}$$

$$\frac{\partial \phi_{L,i}}{\partial t} + \frac{\partial u_L \phi_{L,i}}{\partial z} = D_L \frac{\partial}{\partial z}\left(\varepsilon_L \frac{\partial C_{L,i}}{\partial z}\right) + k_{L,i}a(C_i^* - C_{L,i}) + \varepsilon_L R_i \tag{2}$$

$$\varepsilon_G + \varepsilon_L = 1 \tag{3}$$

Eqs. (1) and (2) are partial mass balance for each species, i transported in gaseous and liquid phase respectively. u_G and u_L are the gas and liquid velocities, respectively. ε_G and ε_L are the volume fraction of the gas and liquid phase summing at one, as stated in Eq. (3). $C_{G,i}$ and $C_{L,i}$ are the concentration of species i per unit volume of the gas and liquid phase respectively. Hence, $\phi_{G,i}$ is the concentration of species i present in the gas phase per unit volume of the column, i.e. $\phi_{G,i} = \varepsilon_G C_{G,i}$. Similarly, $\phi_{L,i} = \varepsilon_L C_{L,i}$ holds for the same species in the liquid phase. R_i is the volumetric consump-

tion/production rate per unit volume of liquid ($mg_i \cdot L^{-1} \cdot s^{-1}$). D_G and D_L stand for the dispersion coefficient in each phase. The mass transfer rate is obtained from the product of a species dependent mass transfer coefficient, $k_{L,i}$, the interfacial area per unit volume of the column, a, and the driving force ($C_i^* - C_{L,i}$).

In these equations, any variable, $\psi \in \{\phi, u, \varepsilon, C_i, C_i^*, k_L, a, R\}$ actually refers to $\psi(z, t)$ a spatio-temporal dependent variable at any instant time t and with $z = 0$ and $z = H$ corresponding to inlet and outlet conditions respectively. Additionally, $\psi(z, t_\infty)$ refers to the local value of ψ at any z-coordinate at steady-state. Finally, $< \psi(z, t) >$ indicates the spatial average at time t.

Noted that ε_G and ε_L in Eqs. (1) and (2) are defined in the temporal and spatial derivatives, which is not the case for some model proposed in the literature to treat the two-way coupling (Inkeri et al., 2018; de Medeiros et al., 2020; Li et al., 2019). These models used empirical or semi-empirical correlations to describe the coupling of hydrodynamics and mass transfer, with the parameters of these correlations usually obtained via spatial-dependent local values, typically calculated through global mass balance (Inkeri et al., 2018; Li et al., 2019).

2.1.2. Closure equations

Besides the resolved variables $\phi_{L,i}$ and $\phi_{G,i}$, closure equations or additional models are needed to define the parameters in the conservation equations. Theses closures parameters reflect the local physical phenomena occurring on the non-resolved scale of the axial 1D model.

Dispersion coefficients: D_G is related to large velocity differences between the bubbles of different sizes (Bardin-Monnier et al., 2003). D_L describes the mixing in the liquid phase, attributed to different reasons such as large-scale liquid recirculation, radial exchange flow, bubble-induced agitation and liquid entrainment induced by density gradient (Deckwer and Schumpe, 1993). These recirculation flow induce an axial mixing and appears mostly under heterogeneous regime (Heijnen and K. Van't Riet, , 1984). Different correlations exist in the literature to estimate D_G and D_L (Heijnen and Van't Riet, 1984; Wachi and Nojima, 1990). Here, D_L is estimated from the correlation of (Deckwer et al., 1974) and it was kept constant throughout the column. D_G is estimated from the correlation of (Wachi and Nojima, 1990) and it was also kept constant for the sake of simplicity. These coefficients depend on the bubble column diameter (D_r) and the superficial gas velocity (j_G), expressed as:

$$D_L = 2.7 \cdot 10^{-4} \cdot (D_r \cdot 100)^{1.4} \cdot (j_G \cdot 100)^{0.3} \tag{4}$$

$$D_G = 20 \cdot D_r^{1.5} \cdot j_G \tag{5}$$

Slip velocity: the expression for the slip velocity valid in homogeneous bubbly flow regime is defined in Eq. (6). It is obtained from a momentum balance on an isolated bubble having reached its terminal velocity and it involves the Sauter mean diameter d_b and a drag coefficient C_D.

$$u_{slip} = u_G - u_L = u_\infty = \sqrt{\frac{4}{3}\frac{g(\rho_L - \rho_G) d_b}{\rho_L C_D}} \tag{6}$$

Various correlations for the drag coefficient, obtained from (Tomiyama et al., 1998), (Mei et al., 1994), and (Dijkhuizen et al., 2010) are implemented in the model. The Tomiyama correlation is valid for slightly contaminated systems, and the two others apply for clean bubbles. These correlations are reported in Appendix A.

Mass transfer term: The mass transfer term changes with the vertical coordinate z because it involves other variables that are spatially dependent ($\varepsilon_G, d_b, u_{slip}$). The local $k_{L,i}$ value is estimated using the correlation of (Higbie, 1935) as written in Eq. (7) and it is species dependent due to different value of liquid-side diffusion coefficient D_i. The local interfacial area is computed from the local gas volume fraction ε_G and the local bubble diameter d_b.

unit ? (m/s)

$$k_{L,i} = 2\sqrt{\frac{u_{slip}D_i}{\pi d_b}} \tag{7}$$

$$a = \frac{6\varepsilon_G}{d_b} \quad \text{the interfacial area per unit volume of the column} \tag{8}$$

The solubility of each species (C_i^*) is set from the Henry constant He_i and the local partial pressure P_i.

$$C_i^* = He_i \cdot P_i = He_i y_i P = He_i C_{G,i} RT \tag{9}$$

Here, it is important to provide more details on the calculation of the local total pressure which depends on the overall gas retention in the volume of fluid above a given location z. It is expressed as:

$$P(z,t) = P_0 + \left(1 - \widetilde{\varepsilon_G(z)}\right)\rho_L g(H - z) \tag{10}$$

with $\widetilde{\varepsilon_G(z)} = \frac{1}{H-z}\int_z^H \varepsilon_G(\zeta, t) \cdot d\zeta$

The volume fraction of the gas phase changes due to mass transfer/bioreaction and pressure dependence on the vertical coordinate z. It is assumed that the number of bubbles per unit volume remains constant throughout the column which leads to the following relationship.

diamètre moyen des particules

$$\frac{d_b^3(z,t)}{\varepsilon_G(z,t)} = \frac{d_b^3(0,0)}{\varepsilon_G(0,0)} \tag{11}$$

Consumption/production rates: R_i

(Schill et al., 1999) proposed that the biocatalysed conversion of hydrogen and carbon dioxide into methane is represented through Eqs. (12) and (13).

$$H_2 + v_{CO_2,1}CO_2 + v_{NH_3,1}NH_3 \xrightarrow{r_1} v_{X,1}X + v_{CH_4,1}CH_4 + v_{H_2O,1}H_2O \tag{12}$$
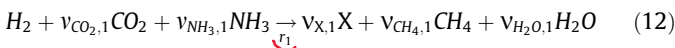
Besides growth, the authors indicate that hydrogen is also consumed to produce maintenance energy, through the following reaction

$$H_2 + v_{CO_2,2}CO_2 \xrightarrow{r_2} v_{CH_4,2}CH_4 + v_{H_2O,2}H_2O \tag{13}$$
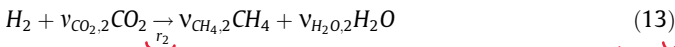
Here, we consider a third reaction, the death of biomass.

$$X \xrightarrow{r_3} \varnothing \tag{14} \quad = X$$

The metabolic flux-based model consists in computing the vector of reaction rates $r = \{r_1, r_2, r_3\}$ in ($g_{H_2} \cdot L^{-1} \cdot h^{-1}$). Let φ_{H_2} be the hydrogen specific uptake rate and m the specific maintenance rate (both in $g_{H_2} \cdot g_X^{-1} \cdot h^{-1}$). In contrast to the work of Schill et al., we do not assume that $r_2 = mX$ (the maintenance rate is no longer constant) and we alternatively use m to set the upper bound for the maintenance reaction rate ($r_2 \in [0, mX]$). The second constraint is $r_1 + r_2 = \varphi_{H_2}X$. Finally, the priority is given to the maintenance reaction.

$-g_X > g_{H_2} g_X^{-1} h^{-1}$ ok

$$\varphi_{H_2} > m \rightarrow r = \{\varphi_{H_2} - m, m, 0\} \cdot X \quad \longrightarrow \text{Production de CH4} \tag{15}$$
$$\varphi_{H_2} < m \rightarrow r = \{0, \varphi_{H_2}, m - \varphi_{H_2}\} \cdot X \quad \longrightarrow \text{pas de production CH4}$$

As a consequence of the calculation procedure (15), growth is only possible if the maintenance requirement is met ($\varphi_{H_2} > m$) and, in that case, the death rate is negligible. Otherwise, if the

hydrogen supply is insufficient to satisfy the energy demand for maintenance ($\varphi_{H_2} < m$), growth stops, maintenance proceeds at a rate defined by the hydrogen uptake rate φ_{H_2} and the cell death rate is proportional to the energy lacking for maintenance.

The calculation of the hydrogen specific uptake rate, φ_{H_2}, uses basic principles of multiphase reactive systems: the reaction rate in the suspended (biological) phase is either set by the kinetics in that phase or limited by the external (physical) transport rate. Considering that the physical transport of substrate precedes uptake by the microorganisms, i.e. the two phenomena occur in series, the actual consumption rate can be expressed as the rate of the limiting step: biological consumption or physical transport rate (Morchain et al., 2017). A standard approach in multiphase reactor modeling is to define the actual consumption rate as the smallest of the two rates.

$$\varphi_{H_2} = \min\left\{\varphi_{bio}, \varphi_{phy}\right\} \tag{16}$$

The biological specific uptake capacity is set from the maximum hydrogen uptake capacity $q_{H_2}^{max}$, and the hydrogen concentration in the liquid phase C_{L,H_2}, through a Monod type equation.

$$\varphi_{bio} = q_{H_2}^{max} \cdot \frac{C_{L,H_2}}{K_{H_2} + C_{L,H_2}} \tag{17}$$

The physical transport rate, φ_{phy} in Eq. (18) involves two phenomena: the gas–liquid mass transfer and the micromixing (responsible for the transport of dissolved species toward the cell-liquid interface). These phenomena are in parallel and the specific mass flux supplied to the cell is therefore set by the largest of the two rates, as expressed in Eq. (18):

$$\varphi_{phy} = max\left(\frac{k_L a_{H_2}(C_{L,H_2}^* - C_{L,H_2})}{\varepsilon_L X}, \frac{C_{L,H_2}}{X.\tau_m}\right) \tag{18}$$

In the limit of the local dissolved hydrogen going to zero, the physical supply is set by the specific gas–liquid mass transfer rate. Otherwise, the physical supply is set by the rate of micromixing in the liquid phase (τ_m). In this work, it is set to 0.01 s. This second term is needed in the case where the local interfacial area would approach zero, for any reason, at some location, during the calculation. Altogether, Eqs. (15)–(18) provide a physically consistent and numerically stable way to include a non-constant maintenance rate in the modelling. It thus improves the model of (Schill et al., 1999) (constant maintenance rate) and avoids the introduction of new arbitrary parameters in additional damping functions, as proposed by Inkeri et al. (2018) (Eqs. (46) and (47) in the cited paper).

In the end, the reaction terms per unit volume of liquid, in Eq. (2), are computed as

$$\begin{aligned} R_{H_2} &= r_1 + r_2 = \varphi_{H_2}X \\ R_{CO_2} &= Y_{CO_2/H_2}r_1 + Y_{CO_2/H_2}^m r_2 \\ R_{CH_4} &= Y_{CH_4/H_2}r_1 + Y_{CH_4/H_2}^m r_2 \\ R_X &= Y_{X/H_2}(r_1 - r_3) \end{aligned} \tag{19}$$

$Y_{i/j}$ is the yield coefficient in gram of i per gram of j consumed. The values of all biological parameters reported in Table 1 are taken from the work of (Schill et al., 1999). M_i is molar mass of species i.

The consequences and advantages of this formulation are further detailed in the last part of the discussion section dedicated to the fully coupled simulation of an industrial scale methanation bubble column.

To sum up the proposed 1D model relies on the following choices and assumptions:

Table 1
Biological parameters.

Parameters	Definition	Value	Units
Y_{X/H_2}	$v_{X,1} \frac{M_X}{M_{H_2}}$	0.22	g_X/g_{H_2}
Y_{CO_2/H_2}	$v_{CO_2,1} \frac{M_{CO_2}}{M_{H_2}}$	5.70	g_{CO_2}/g_{H_2}
Y_{CH_4/H_2}	$v_{CH_4,1} \frac{M_{CH_4}}{M_{H_2}}$	1.92	g_{CH_4}/g_{H_2}
Y_{CO_2/H_2}^m	$v_{CO_2,2} \frac{M_{CO_2}}{M_{H_2}}$	5.5	g_{CO_2}/g_{H_2}
Y_{CH_4/H_2}^m	$v_{CH_4,2} \frac{M_{CH_4}}{M_{H_2}}$	2	g_{CH_4}/g_{H_2}
$q_{H_2}^{max}$	Maximum H_2 specific uptake rate	1.77	$g_{H_2}/g_X/h$
m	Maintenance rate	0.14	$g_{H_2}/g_X/h$
K_{H_2}	Affinity constant	0.01	mg_{H_2}/L

i. One dimensional two-phase flow in homogeneous bubbly flow regime
ii. Constant bubble number without breakup and coalescence
iii. Interfacial bubble contamination considered in the drag law formulation
iv. Hydrodynamics & multispecies mass transfer & bioreaction multiple-way coupling
v. Potential limitation of biological uptake rates by gas–liquid mass transfer

2.2. Numerical resolution

Partial differential equations (1) and (2) are solved using the finite difference method on a regular grid with N nodes, so that the solution is approximated by the vector of discrete values $\phi_{G,i,n}$ and $\phi_{L,i,n}$ where $n \in [1,N]$. A second order discretization in space is used for transport equations and boundary conditions, i.e. the convection term is calculated using second order upstream differences and the dispersion term is calculated using second order central difference, similar to the work of Giovannettone and Gulliver (2008). The spatial discretization of Eqs. (1) and (2) leads to a system ordinary differential equation which is solved using the MATLAB 2017b stiff solver ode15s.

$\frac{d\phi_G}{dz}\big|_{z=L} = 0$

Boundary and initial condition:
Dirichlet boundary condition for the gas mass flow rate, ϕ_G is imposed at the inlet, whereas zero-slope boundary condition is imposed at the outlet. As the simulated bubble columns operates in semi continuous mode, a zero-flux boundary condition is imposed for ϕ_L at the inlet and the outlet. The initial condition for the gas phase is computed based on the ideal gas law using spatially dependent pressures. Whereas, for the liquid phase, ϕ_L is initialized to 0, indicating the absence of dissolved gas components initially for instance.

$\frac{d\phi_L}{dz}\big|_{z=0, z=L} = 0 \qquad \frac{d\phi_G}{dz}\big|_{z=0} = x$

Numerical procedure:
The set of equation is actually algebro-differential since the calculation of the right-hand terms in Eqs. (1) and (2) require that the retention and concentrations of all species in each phases are retrieved from the known $\phi_{G,i,n}$ and $\phi_{L,i,n}$. These $(2i+1).N$ unknowns are solution of a non-linear system (20) which connects hydrodynamics and mass transfer to the local pressure calculated using Eq. (10).

$$\begin{cases} \phi_{G,i,n} = \varepsilon_{G,n} \cdot C_{G,i,n} \\ \phi_{L,i,n} = (1 - \varepsilon_{G,n}) \cdot C_{L,i,n} \\ \frac{P_n}{R.T} = \sum_i \frac{C_{G,i,n}}{M_i} \\ P_n = P_0 + (1 - \widetilde{\varepsilon_G}) \rho_L g(H - z_n) \end{cases} \quad n \in [1,N] \qquad (20)$$

Thus, the non-linear system (20) resolution as explained in Appendix B is embedded within the time stepping procedure presented in Fig. 1 to provide the local retention and concentrations of each species in both phases at every grid point.

The resolution starts with the preprocessing of the problem: specifying the reactor geometry, the operating conditions, the species involved, and defining boundary and initial conditions. The non-linear system of Eq. (20) is solved iteratively until the relative difference of ε_G, $C_{G,i}$, and $C_{L,i}$ between consecutive iterations (*Crit*) is below the given tolerance (*Tol* = 10^{-6}). The bubble diameter and slip velocity are updated (Eqs. (11) and (6) respectively) and used to compute the right hand side of Eqs. (1) and (2). In the end, time integration is performed by MATLAB solver.

2.3. Experimental setup

Among the model's input, d_b is not modellable. A series of experiment was therefore conducted in a lab-scale bubble column with tap water to obtain the Sauter mean diameter d_{32} of the equivalent sphere diameter which serves as an inlet parameter, $d_b(0,t)$. Some results on d_{32} are shown in Appendix C. Alongside with the bubble size measurement, the corresponding gas holdup was also measured dynamically in order to validate the hydrodynamics aspect of the model.

The experimental setup is shown in Fig. 2. It is composed of a 22 L glass cylinder column (3) with a diameter of 0.15 m. The initial liquid height (H_0) is kept at 1 m. Bubbles are injected through a ceramic porous plate with a porosity of 100–160 μm at the bottom of the column occupying the entire section of the column in order to favor homogeneous flow regime in the column. The gas feed line is equipped with a flowmeter (4) with measuring range of 0–2 NL/min. A camera, Cam1 (1) was installed at column's mid-height to identify the bubble geometrical characteristics. A second camera, Cam2 (2) was placed at the free-surface to detect the rising water level for the gas holdup calculation. Cam1 provided an acquisition window of 26×26 mm^2 with a spatial resolution of 40-pixel mm^{-1}. Cam2 has a narrower but longer view of 9.7×38.7 mm^2 with a spatial resolution of 27-pixel mm^{-1}. Cam2 and Cam1 operated simultaneously at the same frequency of 20 Hz with a total of 1000 images shot for each measurement. A homogeneous light-emitting diode (LED)-panel was installed behind the column to increase the luminosity.

2.3.1. Bubble size and dynamic gas holdup measurement

Tap water was used as the liquid phase and H_2 was used as the gas phase. H_2 was chosen to study the column hydrodynamics because of its very low solubility which guaranties that the mass transfer effect on hydrodynamics is minimal.

Pictures of the rising water level were taken near the column wall to reduce the negative effect of the continuous disturbance of the unalterable changes between the refractive indices due to the curved surface of the glass column. The superficial gas velocity, $j_G = Q_G/S$ defined as the gas flow rate (Q_G) per column cross-section (S) was varied between [0–0.16] cm/s. The recorded images from both cameras were then treated using Matlab®.

The image processing algorithm used to extract the bubble geometrical characteristics followed the methodology of Laupsien et al. (2019). Bubble images and its associated experimental results are provided in Appendix C. The dynamic gas holdup was measured using bed expansion method but a camera was applied rather than a ruler to better capture the liquid swelling. The algorithm to determine the global gas holdup is depicted in Fig. 3. 64-
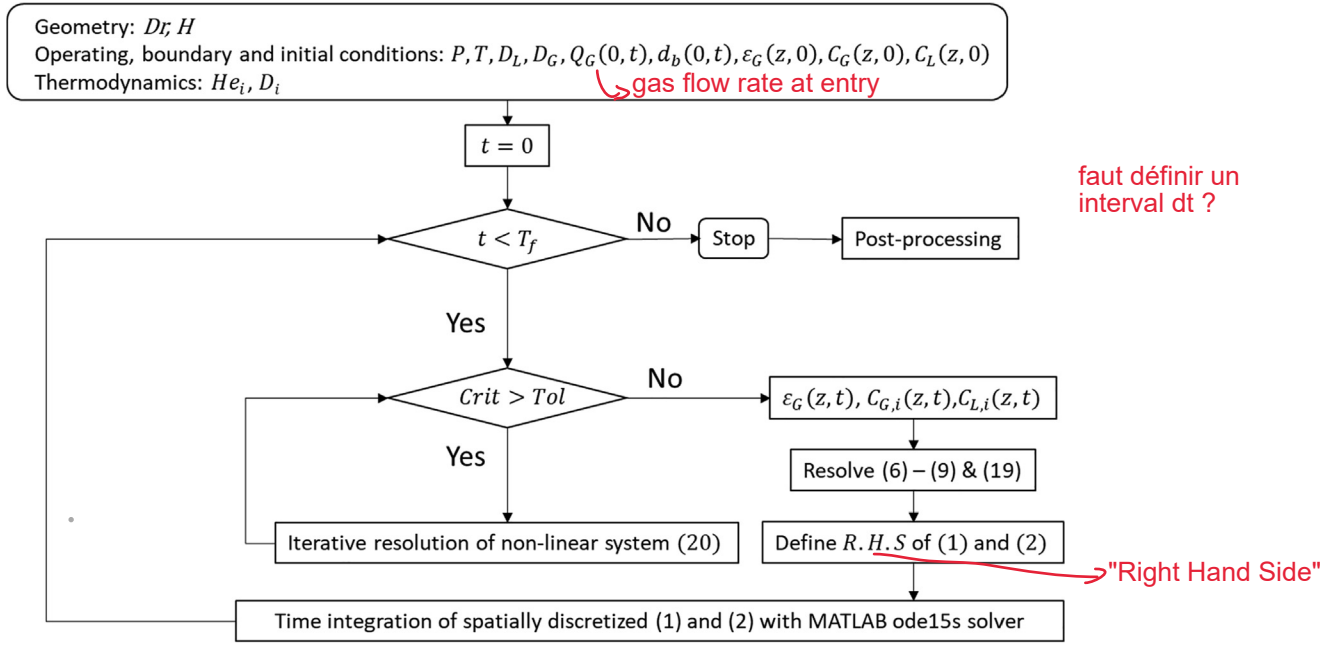
Fig. 1. Algorithm flowchart for the resolution of the model.
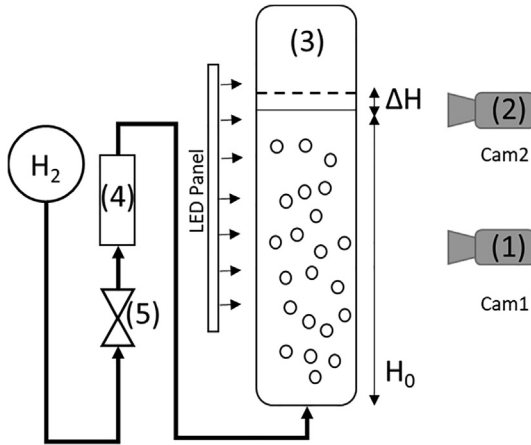

Fig. 2. Experimental setup for gas holdup and bubble size measurements.

pixel column nearest to the wall were extracted to calculate the mean pixel value for each level. The profile obtained was then normalized so that all images was compared to the same threshold value. The lower meniscus level was detected by applying a threshold of 70% of the maximum pixel value. The process was repeated for all images to obtain the water level time profile. The difficulty of this method lies in identifying the water level when the first bubble reaches the free surface. Indeed, the water level profile becomes chaotic when the bubbles reach the free liquid surface and, from that point onward, exploiting the real water level height is tedious, due to foaming. We chose to track the water level change, ΔH, until the first bubble reaches the free surface. In order to prove that the difference between these two methods is insignificant, the cumulative statistical average of ΔH at steady state was compared to the ΔH upon arrival of the first bubble and the difference was quantified. A relative difference of less than 5% was found, even for gas holdup below 1%. The details on the comparison is elaborated in Appendix D. For this reason, the ΔH was con-

sidered until the image on the arrival of bubbles at the free surface. Moreover, the precision of the method can be improved by increasing the camera speed to better capture the last instant before the perturbation of the water level by the bubbles. Besides, the flow rate studied is low (j_G below 0.16 cm/s with reactor diameter of 0.15 m), the column is operated in the homogeneous bubbly flow regime, with weak liquid circulation, according to (Shah et al., 1982) regime map. (Sasaki et al., 2017) employed a very similar method for the study of gas holdup. However, the gas flow rate in Sasaki et al. work is rather high and the flow regime is heterogeneous with large liquid recirculation. The establishment of the flow regime, leading to constant gas holdup, is much longer in their case.

The experimental gas holdup was then calculated using Eq. (21). In this equation, H_0 corresponds to the initial liquid height and $\Delta H(t)$ holds for the instantaneous liquid elevation ($H(t) - H_0$), as shown in Fig. 2. It was found experimentally that the slope of the rising water level profile corresponds to the superficial gas velocity. The abovementioned methods are non-intrusive way of direct and concise measurement of both bubble size, superficial gas velocity, and global gas holdup simultaneously.

$$\langle \varepsilon_{G,exp}(t) \rangle = \frac{\Delta H(t)}{\Delta H(t) + H_0} \tag{21}$$

$$j_G = \frac{Q_G}{S} = \frac{\Delta H}{\Delta t} \tag{22}$$

2.3.2. Comparison with model

The H_0, Q_G and experimentally measured bubble size were used in the model as inlet parameters. The gas holdup at the inlet is computed as the ratio between the superficial gas velocity and the u_{slip} from Eq. (6). Different drag laws were tested and the model prediction compared with experimental data. As already mentioned, a measurement of dynamic gas holdup allows to evaluate both the superficial gas velocity (from the slope in Fig. 3) and the final gas holdup. The former serves as a check of gas flow rate applied experimentally and the latter can be compared to that pre-
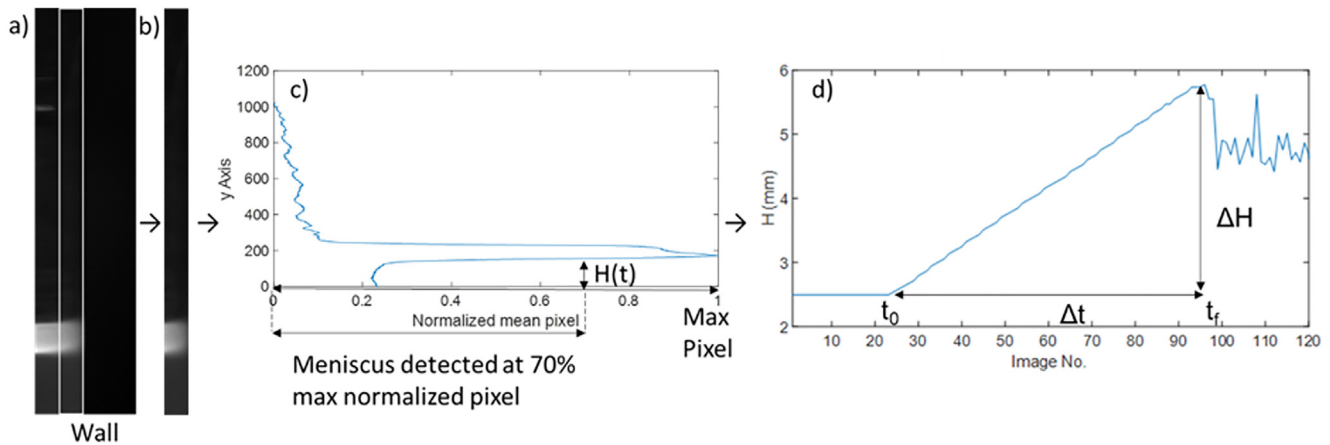
Fig. 3. Global gas holdup measurement from image processing of raw data. (a) Raw image (b) Cropped image (c) Normalized pixel profile (d) Instantaneous liquid level.

dicted by the model. The $\langle \varepsilon_{G,exp} \rangle$ was compared with the global gas holdup given by the model, $\langle \varepsilon_G(z, t_\infty) \rangle$ which is the total spatial average of gas retention at steady-state. The model is also expected to reproduce the dynamic evolution of $\langle \varepsilon_{G,exp} \rangle$. This approach is similar to (Besagni et al., 2019) work whereby, the bubble size experimental measurements served as inlet conditions for the numerical CFD model and the model's gas holdup was compared to that of experiment.

To mimic the experimental conditions, whereby the global gas holdup is followed dynamically, the following model parameters, initial and boundary conditions are set for the model. The initial gas holdup in the column from node 2 to N (except the inlet, reserved for the boundary condition) was fixed to a relatively small value of 10^{-6} rather than 0; on one hand to represent the absence of gaseous phase initially in the column and on other hand to facilitate the numerical convergence and to reduce initial stiffness. The outlet pressure, $P(H, t)$ was kept constant as the atmospheric pressure of 1 atm.

3. Results

3.1. Hydrodynamics validation through transient gas holdup measurement

A key feature of the model is its ability to describe spatio-temporal changes in the gas retention and bubble diameter through which the evolution of interfacial area can be predicted. This section is devoted to the validation of the transport terms of our equation through a comparison of the model results with the experimental measurement of gas holdup in the transient period following gas injection in a column initially filled with liquid.

The results presented in Fig. 4 indicate that the gas retention increases linearly in time. The slope of the experimental curve corresponds to the superficial gas velocity: imposed gas flow rate divided by the column cross section. The numerical slope also closely matched that of experiment.

The slope of the simulated retention curve given is fully determined by the superficial gas velocity. This slope is independent of the bubble slip velocity. The bubble slip velocity actually defines the gas retention at steady state. The drag law dependent bubble slip velocity sets the gas residence time.

This case was investigated with three different drag laws. Mei model did not fit well as it is more applicable to spherical bubbles. Spherical bubbles rise in a rectilinear manner, hence it has higher bubble velocity and a lower residence time, which explain a lower
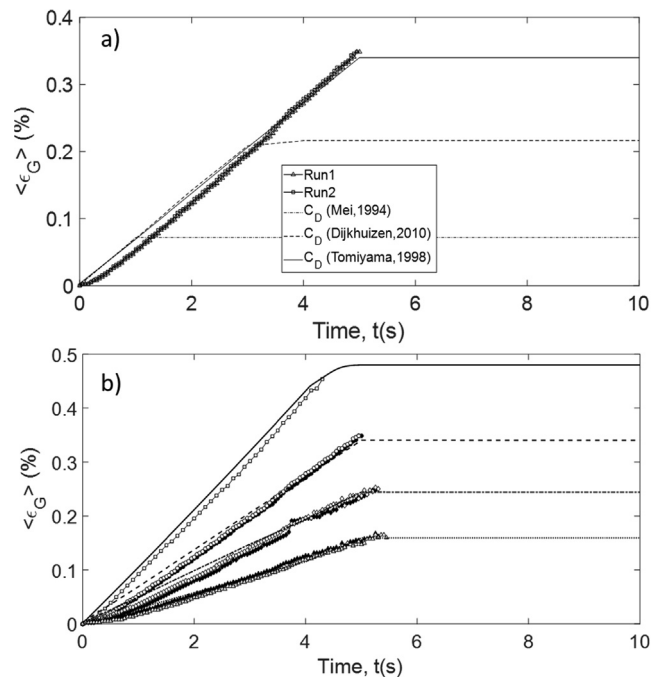
Fig. 4. (a) Experimental and model predicted dynamic gas loading with different drag model. The repeatability is very good. (b) Examples of experimental and model predicted dynamic gas loading using Tomiyama drag model (Tomiyama et al., 1998).

final retention value (Tomiyama et al., 1998). The correlation proposed by (Dijkhuizen et al., 2010) are more suitable for ultrapure medium, which clearly is not the case of tap water. Therefore, the drag force is less important than that calculated from Tomiyama, hence the bubble velocity is much higher, thus a lower final gas holdup. As expected, Tomiyama correlation has the best fit for our cases as the quality of water used is similar to ours. Tomiyama drag model is applicable for a wide range of conditions, such as different fluid properties and bubbles size, which is the reason why it was used for different simulation cases to be presented in Section 4.

The model yields a good agreement with the experimental measured gas holdup as the relative error between the two is less than 10% (for very low gas holdup, i.e. less than 0.6%), as shown in Table 2. The good agreement also confirms that collective effects on bubble velocity could be neglected at such low gas holdup.

Table 2
Overall experimental and model results.

	j_G (cm/s)	0.039	0.058	0.078	0.105	0.116	0.136	0.155
	d_{32} (mm)	1.76	2.00	2.00	2.20	2.48	2.60	3.15
Experiment	$\langle \varepsilon_{G,exp} \rangle$ (%)	0.16	0.25	0.35	0.45	0.48	0.54	0.59
Model	$\langle \varepsilon_G \rangle$ (%)	0.16	0.24	0.34	0.47	0.49	0.55	0.57

This work demonstrated the present method is suitable to measure extremely low gas holdup. To the authors' best knowledge, the measurement of such low global gas holdup (<0.6%, j_G between [0–0.16] cm/s) is rare in the literature. The closest works were reported by Kováts et al., Chen & Brooks and Besagni et al. whereby the minimum j_G tested were 0.007 cm/s, 0.15 cm/s, and 0.4 cm/s respectively (Chen and Brooks, 2021; Kováts et al., 2020; Besagni and Inzoli, 2016). To conclude this experimental section, the proposed dynamic gas holdup measurement yields a very neat slope during gas loading which corresponds to the superficial gas velocity imposed at the inlet and it quantifies the global gas holdup at steady-state via optical means without perturbating the hydrodynamic flow.

3.2. Local mass transfer validation through experimental axial measurement

Our model is further used for the simulation of CO_2 mass transfer in a large-scale bubble column (H = 4.4 m) fed with a liquid flow rate of 3 m³/h, operated in co-current mode. The local gas holdup and local CO_2 profile measured by (Deckwer et al., 1978) is used to validate our model. Similar work has been reported by Hissanaga et al. (2020) and Rzehak and Krepper (2016). In fact, (Rzehak and Krepper, 2016) pointed out that local measurement of both concentration and bubble size distribution is scarce in the literature, which makes this work very meaningful for the validation of our model. In all these works, the reaction of CO_2 with water was neglected, the same assumption is made here. The temperature is set as 14 °C. The CO_2 liquid diffusivity D_{CO_2} and Henry constant He_{CO_2} at this temperature is calculated from the expression given by (Versteeg and Van Swaaij, 1988) which yield $1.4663 \cdot 10^{-9}$ m²/s and 0.0192 mg/L/Pa respectively.

Fig. 5 and Table 3 show the results of our model compared to that of Hissanaga et al. 1D model and Deckwer et al. experimental data. For our model, the inlet bubble diameter was taken the same as experimental value measured by Deckwer et al., which equals to 2.86 mm for the two flow rates. Following the work of Hissanaga et al., plug flow condition is supposed for both phases. Therefore, D_L and D_G are equal to 0 in this particular case. In Fig. 5a, the local gas holdup varies noticeably with axial location due to large column size and high interphase mass transfer rates. For experiment 17, the local gas holdup decreases at the bottom of the column due to an intense gas to liquid mass transfer flux. Then, the local gas holdup reaches a minimum and increases again as one approaches the surface. A similar trend is also observed in the X_{CO_2} profile. This reveals that the gas–liquid mass transfer first operates from gas to liquid at the bottom of the column, then in the opposite way in the upper part. Obviously, the gas holdup, the interfacial area and $k_L a$ are not constant and making such hypothesis negatively impacts the prediction of reactor performances in an industrial bubble column. It is interesting to see that both models fail to represent the retention profile of experiment 19. This is because, both models are valid in the homogeneous bubbly flow regime whereas experiment 19 was conducted near the transition regime where some coalescence could occur and increase the mean Sauter bubble diameter and bubble velocity, thus a lower gas holdup. Nevertheless, both models capture reasonably well the local CO_2 profile. Our model slightly overestimates the absorption CO_2 flux at the inlet because

our $k_{L,i}$ value is calculated from the Higbie correlation which gives a slightly higher value than the correlation used by Hissanaga et al. Lastly, the outlet flow rate ($j_{G,out}$) and the outlet CO_2 mass fraction are correctly quantified by our model, as shown in Table 3, which shows that our model is capable to reproduce large-scale hydrodynamics and spatially dependent mass transfer rate. In our model, oxygen (O_2) is treated as an active species together with CO_2, which is not the case in Hissanaga et al. model. However, the O_2 mass transfer has not any huge impact on the results. This confirms their hypothesis that O_2 can be treated as an inert species for the mass transfer in this case.

To conclude Section 3, our 1D model is validated temporally and spatially through own-experimental data and literature data.

4. Discussion on multispecies mass transfer/bioreaction

In Section 4, the link between reactor's design, operating conditions and the intensity of multispecies mass transfer is investigated. First, the effect of column's height is studied. Secondly, H_2 mass transfer is studied at two different heights. Next, the effect of multi-species mass transfer is explored with its sensitivity to column's height. In the related Sections 4.1 and 4.2, all the simulations utilized d_b = 2.5 mm at the inlet, in order to facilitate a direct comparison between the results. Finally, a full-scale biological methanation reactor is simulated.

4.1. Case 0: Effect of hydrostatic pressure on interfacial area

Two bubble columns of H = 2 m and H = 10 m fed with the same molar flow rate and operated at $P = 1\,atm$, are simulated using 20 nodes and 100 nodes grid respectively. In this section, the mass transfer coefficient k_L is set to zero. Steady-state results are presented in term of normalized vertical profiles in Fig. 6c and d and global mass balances in Table 4. In Table 4, the local and instantaneous molar flux of species i is calculated as:

$$F_i(z,t) = \frac{y_i(z,t) \cdot P(z,t) \cdot Q_G(z,t)}{R \cdot T} \tag{23}$$

Fig. 6a and b also show that the time to reach a steady state is roughly equal to the bubble residence time (H/u_{slip}). This is consistent with the fact that the pressure-induced changes in bubble diameter have little effect on the rising velocity in the present case. For H = 2 m and H = 10 m, bubble diameter ranges in [2.5–2.7] mm and in [2.5–3.2] mm respectively (graph not shown) leading to u_{slip} approximately constant when using Tomiyama drag correlation. The effects of bubble expansion due to decreasing pressure however explain the slightly non-linear $\langle \varepsilon_G \rangle = f(t)$ and $\langle a \rangle = f(t)$ curves in the 10 m high column. At steady-state, the changes in gas retention and interfacial area with height are much more pronounced in the tall column than in the small column and the spatial profile is clearly non-linear. The hydrostatic pressure decreases with decreasing height, which causes an expansion in gas volume, hence, the gas holdup increases. This implies, in the same time, an increase in bubbles size due to Eq. (11). Similar observations are reported in the experimental study of Giovannettone et al. (2009).

We compare the interfacial area, $\langle a(z, t_\infty) \rangle$, and its approximation based on averaged quantities $6\langle \varepsilon_G \rangle / \langle d_b \rangle$. Results are reported
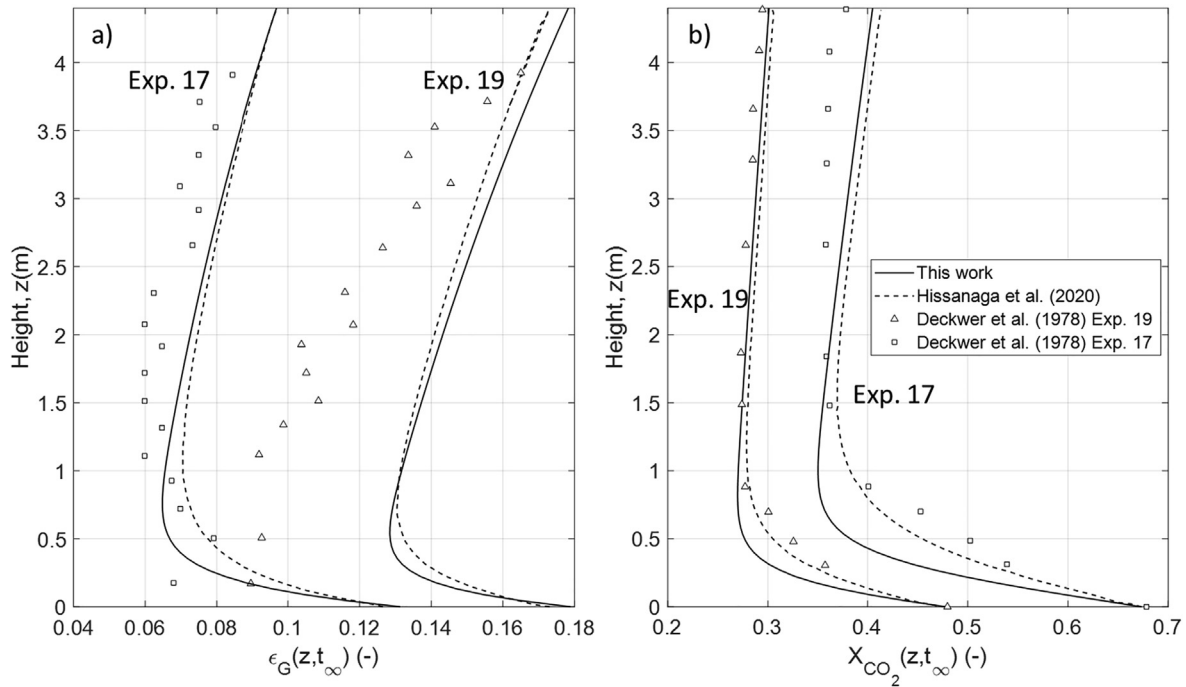
Fig. 5. (a) Local gas holdup and (b) local gaseous CO_2 mass fraction (X_{CO_2}) at steady-state. □: Experiment 17 and Δ: Experiment 19.

Table 3
Model output compared to Deckwer et al. experimental work and Hissanaga et al. 1D model.

Exp.	$j_{G,in}$ (cm/s)	Deckwer et al. (1978)		Hissanaga et al. (2020)		This work	
		$j_{G,out}$ (cm/s)	$X_{G,out}$ (−)	$j_{G,out}$ (cm/s)	$X_{G,out}$ (−)	$j_{G,out}$ (cm/s)	$X_{G,out}$ (−)
17	3.42	2.49	0.377	2.62	0.413	2.58	0.405
19	4.63	4.59	0.293	4.64	0.306	4.58	0.301

in Table 4. Note that if $\langle \varepsilon_G \rangle$ is accessible in experiments, the information about $\langle d_b \rangle$ is much difficult to obtain in an industrial scale column. In a 10 m high column, the relative error between $\langle a(z,t_\infty) \rangle$ and $6\langle \varepsilon_G \rangle / \langle d_b \rangle$ is only 1% because the change in diameter due to hydrostatic pressure is negligible. However, nonlinearities are more pronounced in tall columns and the evaluation of mass transfer related quantities from global measurements becomes a risky exercise in real systems.

### 4.2. Two-way coupled hydrodynamics and mass transfer problem

4.2.1. Case 1: Effect of hydrostatic pressure on H_2 mass transfer

Case 1 evaluates the impact of scale-up on the H_2 mass transfer (a weakly soluble gas) in two columns fed with the same constant gas molar flow rate as in Case 0 (column diameter $D_r = 0.15$ m). The mass transfer term is now activated and the initial hydrodynamic conditions are taken from the converged hydrodynamics of case 0. This represents the experimental situation when the column is initially fed with an inert gas at t < 0 and the switch to a transferable gas is performed at t > 0 without perturbating the hydrodynamics. The model parameters D_L and D_G, set through Eqs. (4) and (5) are provided in Table 4. The temperature is set as 25 °C. The H_2 liquid diffusivity D_{H_2} and Henry constant He_{H_2} at this temperature are taken as $5.1488 \cdot 10^{-9}$ m^2/s and $1.56 \cdot 10^{-5}$ mg/L/Pa respectively (Sander, 2015).

The gas holdup, bubble size and interfacial area profiles are not shown as they remain the same as that of case 0. This is expected since the solubility of H_2 is extremely low and the hydrodynamics

is not impacted by the H_2 mass transfer (one-way coupling case). From this information and using concentration profiles, the local mass transfer fluxes are computed and presented in Fig. 7c.

Intuitively, the global mass transfer rate is null when a bubble column operated in semi-continuous mode reaches a steady-state. The liquid phase gets saturated by the dissolved gas components leading to $C_L = C^*$ throughout the column. Fig. 7c depicts that the global mass transfer is indeed null whilst the mass transfer flux evolves spatially even at steady-state. From Fig. 7a the C_{G,H_2} is higher at the bottom of the 10 m high column due to the elevated hydrostatic pressure whilst the value is identical at the free surface due to the same atmospheric pressure. The linear decrease of C_{G,H_2} due to decreasing local pressure shows that the gaseous phase is spatially heterogeneous. Fig. 7b presents the concentration in the liquid phase as well as the equilibrium concentration C^*. In the 2 m high column, the liquid mixing time at 63% homogeneity is estimated from the analytical solution of Inoue (1973); $\tau_m \approx 140s$ is comparable to the mass transfer characteristic time, $\tau_{tr} = \frac{1}{\langle k_L a \rangle} \approx 150s$, and despite the saturation concentration change, the liquid concentration remains homogeneous throughout the column. For H = 10 m, the liquid concentration profile is non-uniform because of insufficient mixing in the liquid phase ($\tau_m = 3400s \gg \tau_{tr} = 225s$). The mass transfer coefficient is averaged from the value presented in Fig. 8b. Fig. 7b shows that the saturation concentration C^* follows the trend of gaseous concentration. At steady-state, the local C_L are everywhere different from C^*, but the overall mass transfer is zero. Note that the (net transfer flux = 10^{-8}/F$_{in}$ = 10^{-4}). Fig. 7c displays that absorption
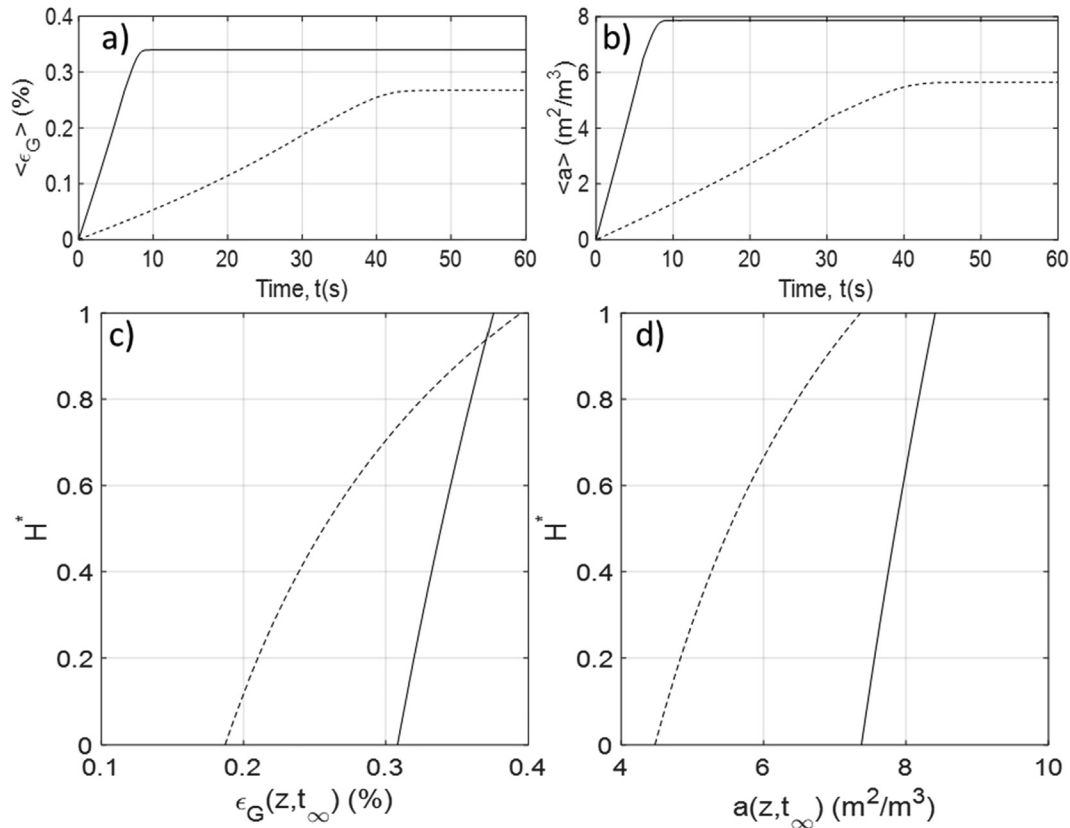
Fig. 6. (a–b) Dynamic simulation of mean gas holdup and interfacial area until steady-state for two column heights. (c–d) Normalized vertical profiles of gas holdup and interfacial area at steady-state. – H = 2 m, − − H = 10 m.

Table 4
Model's input and steady-state hydrodynamic results for two different column's height.

		2	10
Model Inputs	H (m)	2	10
	$F_{H_2}(0,t)$ (10^{-4} mol/s)		6.8286
	$j_G(0,t)$ (cm/s)	0.081	0.049
	D_L (m^2/s)	$5.6 \cdot 10^{-3}$	$4.8 \cdot 10^{-3}$
	D_G (m^2/s)	10^{-3}	$5.7\ 10^{-4}$
Model Outputs	$P(0,t_\infty)$ (Pa)	120,880	199,240
	$F_{H_2}(H,t_\infty)$ (10^{-4} mol/s)	6.8293	6.8293
	$F_{H_2}(0,t_\infty) - F_{H_2}(H,t_\infty)$ (10^{-4} mol/s)	−0.0007	−0.0007
	$\langle \varepsilon_G(z,t_\infty) \rangle$ (%)	0.34	0.25
	$\langle a(z,t_\infty) \rangle$ (m^2/m^3)	7.866	5.65
	$6 \langle \varepsilon_G(z,t_\infty) \rangle / \langle d_b(z,t_\infty) \rangle$ (m^2/m^3)	7.872	5.71

occurs in the lower half of the column, desorption takes place in the upper half. This observation is also reported in Giovannettone's experimental work where positive gas transfer rate was found in the lower part of the column and negative gas transfer rate in the upper part (Giovannettone and Gulliver, 2008). This is an interesting illustration to the fact that macroscopic observations (the net transfer rate is equal to zero) cannot be used to infer local phenomena (the local mass transfer rate is nowhere equal to zero).

A benefit of the spatially discretized model is the opportunity to compute the integral mass transfer over the total column height or over sub intervals. The global mass transfer rate, T_i (g/s or mol/s) is computed through Eq. (24) as the integral of local mass transfer rate (the spatial reference to z for each variable is omitted for clarity).

$$T_i = S \cdot \int_0^z k_L a \cdot (C_i^* - C_{i,L}) \cdot dz \tag{24}$$

Due to higher hydrostatic pressure in large column, the mass transfer rate is 2 times higher than that at small column, as indicated in Table 5. For the same inlet molar flow rate, the mass transfer is enhanced due to column height. Thus, it can be claimed that it is advantageous to have higher column for low soluble gas as used in biological methanation.

*4.2.2. Case 2: Effect of CO_2 ($y_{CO2,in}$ = 20%) on H_2 mass transfer*

For case 2, the impact of scale-up on the multispecies mass transfer, especially the substrates involved in biological methanation process: H_2 & CO_2 is studied. The model parameters, initial and boundary conditions are the same as case 1. The proportion of H_2:CO_2 is set to 4:1 as the condition usually found in the study of biological methanation, which is in line with the reaction stoichiometry (Rusmanis et al., 2019). A constant pH = 7 assumption is made, therefore dissolved CO_2 remain at their CO_2 form. The temperature is again set as 25 °C. The D_{H_2} and He_{H_2} are kept the same as previous case. The CO_2 liquid diffusivity D_{CO_2} and Henry constant He_{CO_2} at this temperature are taken as $2.2884 \cdot 10^{-9}$ m^2/s and 0.0145 mg/L/Pa respectively (Sander, 2015).

The hydrostatic pressure profile remains unchanged due to low gas holdup and it is not presented here. The presence of CO_2 alters the local gas holdup, even at low concentration (here, $y_{CO2,in}$ = 20%). A more significative effect is observed at the large scale. A slight decrease in ε_G is detected near the inlet which is explained by the preferential and significant mass transfer of CO_2 at the bottom of the column. The variation in ε_G implies changes in the interfacial area and thus in the $k_L a$ profile as shown in Fig. 8.

With the same molar flow rate for both reactors, the model revealed very different local gaseous and liquid concentration profiles. Compared to a linear decrease of gaseous concentration pro-
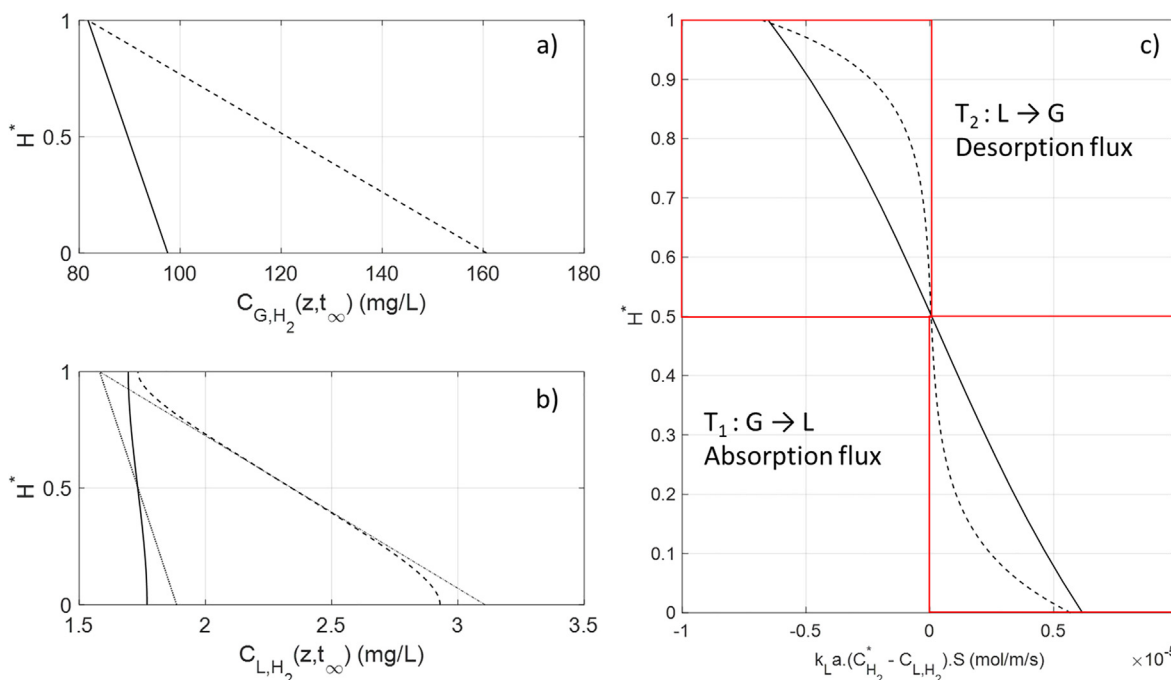
Fig. 7. (a–b) Normalized vertical profiles of concentrations and (c) mass transfer rate at steady-state. Graph legend as follows: $-$ H = 2 m, $- -$ H = 10 m, ■ ■ ■ and $- ■ -$ are C^* profile for H = 2 m and H = 10 m respectively.
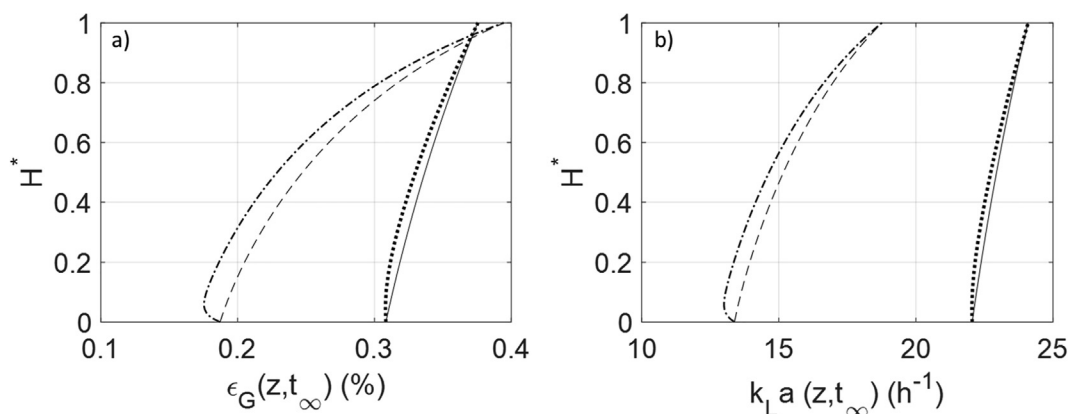
Fig. 8. Normalized vertical profiles ε_G and k_La at steady-state for monospecies, H_2 vs multispecies H_2 & CO_2 for two reactor heights. $-$ and $- -$ are for monospecies cases (case 1: H_2 only) at H = 2 m and H = 10 m respectively. ■ ■ ■ and $- ■ -$ are for multispecies cases (case 2: H_2 & CO_2) at H = 2 m and H = 10 m respectively.

Table 5
Hydrogen local mass transfer fluxes in the lower and upper part of the column.

H (m)	2	10
F_{in} (10^{-4} mol/s)	6.8286	6.8287
T_1 (10^{-4}mol/s)	0.0290	0.066
T_2 (10^{-4}mol/s)	−0.0292	−0.064
$T = T_1 + T_2$ (10^{-4}mol/s)	−0.0002	0.002

file in the absence of CO_2 in Fig. 7a, in this case, the volume contraction due to the intense CO_2 mass transfer (refer to Fig. 9c) causes an enrichment of the gaseous phase in H_2 (see Fig. 9a) at the bottom of the column. An increase in H_2 gas concentration leads to a higher H_2 saturation concentration $C^*_{H_2}$ and consequently increases the hydrogen mass transfer rate. The transfer of the two species is coupled. The phenomenon is amplified in the high column because of stronger pressure effects. Again, the liquid concentration is rather homogeneous at H = 2 m but heterogeneous at

H = 10 m, as shown in Fig. 9b and d. The mass-transfer profile appear to be complex mainly due to the existence of two species with high contrast in terms of solubility (Solubility CO_2 ×100 times higher than that of H_2). Fig. 9e and f reveal that the multi-species mass-transfer effect can be observed even at H = 2 m. Fast dissolution of CO_2 implies high absorption rate at the inlet, but quickly diminished afterward as the liquid concentration approaches the saturation concentration. The strong two-way coupling is clearly exhibited in this example. Non-linear evolution of C^* prompts error in calculating local flux if linear approximation of C^* is used. The estimation of mass transfer flux with the arithmetic mean of C^* will therefore be wrong as C^* profile is no longer linear.

Fig. 9g depicts that the inlet H_2: CO_2 gaseous molar flux ratio of 4:1 is not conserved throughout the reactor as this is caused by the huge contrast in term of solubility. CO_2 is much more soluble than H_2, hence, a huge drop of CO_2 causes an increase of the ratio. As displayed in Table 6, the CO_2 absorption flux ($T_{CO2,1}$) is 6 times higher than that of H_2 ($T_{H2,1}$) at the small scale and also nearly 6
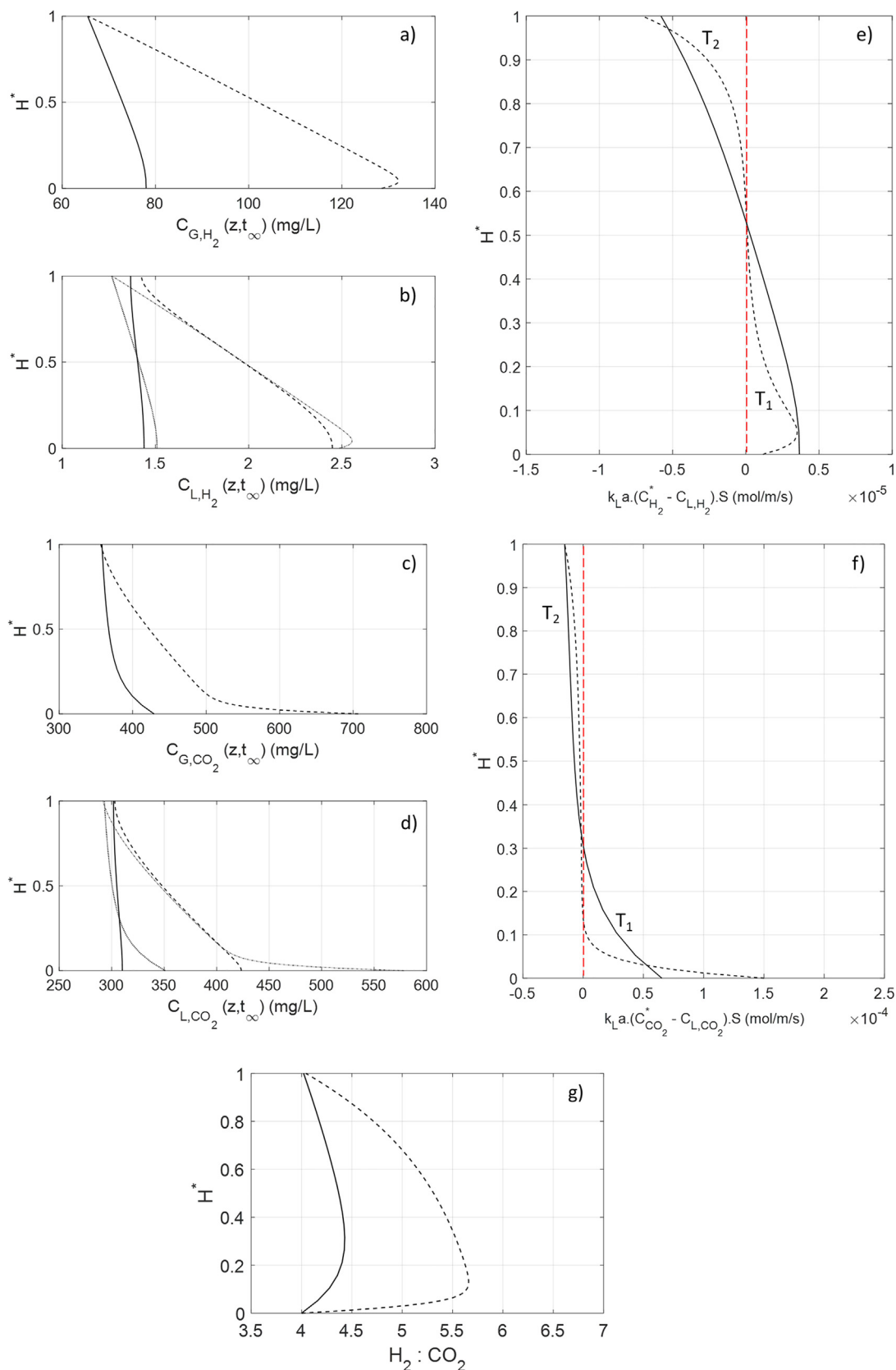
Fig. 9. (a–d) Normalized vertical profiles of gas and liquid concentrations (e–f) Normalized vertical profiles of mass transfer rate, and (g) local H_2: CO_2 ratio at steady-state. Graph legend as follows: − H = 2 m, − − H = 10 m, ■ ■ ■ and − ■ − are C^* profile for H = 2 m and H = 10 m respectively.

times higher at the large scale. Nevertheless, at the small scale, the absorption flux of CO_2 is nearly 10% of the inlet molar flux ($T_{CO2,1}$/

F_{in}), which leads to an increase in the H_2: CO_2 ratio around 10% in the similar way. At the larger scale, the absorption flux of CO_2 rep-

Table 6

H_2 & CO_2 local mass transfer flux.

H (m)	2		10	
Species, i	H_2	CO_2	H_2	CO_2
$F_{i,in}$ (10^{-4} mol/s)	5.463	1.366	5.463	1.366
$T_{i,1}$ (10^{-4} mol/s)	0.023	0.137	0.068	0.410
$T_{i,2}$ (10^{-4} mol/s)	−0.024	−0.131	−0.069	−0.392
$T_i = T_{i,1} + T_{i,2}$ (10^{-4} mol/s)	−0.001	0.006	−0.001	0.018

resents 30% of the inlet molar flux, which results in an even higher H_2:CO_2 ratio.

However, the ratio 4:1 is recovered at the outlet, which is expected, as the net global mass transfer flux is always null at steady-state. The mass transfer profile is different than that of case 1 for H_2 mass transfer (Fig. 9e and f vs. Fig. 7c). Here, it is no longer symmetrical. At the small scale, the only similarity with case 1 is that the H_2 absorption and desorption still occur at the bottom half and the upper half of the column respectively, as shown in Fig. 7c and Fig. 9e. Although the presence of CO_2 alters the linear mass transfer profile (see Fig. 7), the overall mass transfer flux is still conserved. The mass balances for each species are again accurately satisfied as shown in Table 6.

Due to the multispecies mass transfer, the H_2:CO_2 ratio of the absorption flux rate ($T_{H2,1}/T_{CO2,1}$) is 0.023/0.137 = 0.168 and 0.068/0.410 = 0.166 at the small scale and at the large scale respectively. This is far from the expected stoichiometry ratio (4:1). The hydrogen is in large default compared to CO_2, as previously observed by Gerhard and it is repeated in Schill et al. (1999). Gerhard suggested that in order to obtain the ideal stoichiometric proportion of H_2 to $C0_2$ in the liquid phase (i.e., 4:1), the molar ratio between H_2 and $C0_2$ in the gaseous phase has to be greater than 35:1. In this work, we suggest to obtain a stoichiometric proportion in terms of absorption flux to satisfy the biological reaction and not in terms of concentration. In order to better analyze this competition between mass transfer and bioreaction, the next case study addresses biological methanation reaction.

4.3. Case 3: Effect of CH_4 bioproduction on H_2 and CO_2 multispecies mass transfer – Hydrodynamics, mass transfer and bioreaction coupled problem

For the final case, the model is further challenged with an industrial-scale problem including bioreaction. To our best knowledge, the world first full-scale biological methanation demonstration plant is located in Avedore, Denmark (Rusmanis et al., 2019). It operates at a full electrical power load capacity of 1 MW. The reactor is designed to treat up to 50 Nm³/h of CO_2 contained in a mixture of biogas (65% CH_4 and 35% CO_2) issuing from a nearby anaerobic digestor. From a recent study, the objective of the plant is to demonstrate the capability to produce 125 Nm³/h of biomethane at 97% of purity. This is done by upgrading the raw biogas with the addition of 200 Nm³/h of H_2 generated from the hydrolysis of water using the surplus renewable electricity. With these input collected from the literature, it is attempted to use the current model to reproduce the reported results obtained at an industrial scale (Rusmanis et al., 2019; Electrochaea – Carbon and Energy storage, 2017; Electrochaea GmbH, n.d.; Sveinbjörnsson and Münster, 2017). The bubble diameter at the inlet is supposed to be 2 mm as no information is found. A 10-meter high bubble column operated under pressure ≈8 bar and 65 °C, fed with a H_2: CO_2: CH_4 gas molar mixture of 60%:15%:25% was considered. At this temperature, the liquid phase diffusivities of D_{H_2}, D_{CO_2}, and D_{CH_4} are taken as $1.2097 \cdot 10^{-8}$, $5.3765 \cdot 10^{-9}$, and $3.9518 \cdot 10^{-9}$ m²/s respectively. The Henry constants of He_{H_2}, He_{CO_2}, and He_{CH_4} at this temperature is taken as $1.2641 \cdot 10^{-5}$, 0.0056 and $1.0541 \cdot 10^{-5}$ mg/L/Pa respectively (Sander, 2015). Due to a larger column's diameter (0.72 m), the model parameter, D_L is computed as 10^{-1} m²/s by Deckwer correlation. The bioreaction is solved using equations described in Section 2.1.2. (Rafrafi et al., 2020) stated that the increase of pH in ex-situ biological methanation reactor is less problematic than in-situ system. Thus, the effect of pH is not studied and the dissolved CO_2 remain at their CO_2 form, similar to previous works (Inkeri et al., 2018; Markthaler et al., 2020).

In the presence of reaction, the hydrodynamics behavior differs from case 2 (without reaction). The later has already a very distinct hydrodynamic behavior from case 1 (without the presence of CO_2). As depicted in Fig. 10a, the pressure is slightly higher in the presence of bioreaction. The local pressure profile depends on the local ε_G which in turns depends on the mass transfer and the bioreaction. Due to a huge consumption of CO_2 and H_2 (confirmed in Fig. 11a and Fig. 11c), ε_G falls sharply from about 10% to lower than 5% and non-linearly with the height especially in the first half of the column. The impact of bioreaction on the hydrodynamics and the mass transfer is profound, as ε_G reduces almost two-fold because of bioreaction. As expected, this leads to a non-linear decrease in $k_L a$ in a similar manner. Due to high pressure system (P varies between 8 and 9 bar) coupled with high mass transfer flux, it is likely favorable to maintain in homogeneous bubbly flow regime as $\langle \varepsilon_G \rangle$ reaches 6% throughout the column as shown in Fig. 10b.

Fig. 11a and c shows that both H_2 and CO_2 gas concentration plunge and every substrate transferred to the liquid phase is consumed by the reaction to produce CH_4. As presented in Fig. 11b, C_{L,H_2} reaches 0 at the top of the reactor as dissolved H_2 from gas to liquid mass transfer is totally consumed by the bioreaction to form CH_4. Fig. 11d reveals that the dissolved CO_2 is not limiting the reaction as the C_{L,CO_2} is close to its saturation concentration. Dissolved CH_4 is always higher than the saturation C^*, as depicted in Fig. 11f. Therefore, dissolved CH_4 is transferred from the liquid to the gas and C_{L,CH_4} almost reaches the saturation value at the top of the column. The methane concentration in the gas phase is enriched throughout the column, as shown in Fig. 11e, C_{G,CH_4} increases in the same trend as C_{L,CH_4}. From Fig. 11g, the local CH_4 mass transfer profile is opposite of that of CO_2. Moreover, due to the limitation of bioreaction by the H_2 mass transfer at steady state, the local CO_2 transfer is stoichiometrically controlled by the bioreaction: with every 4 mol of H_2 transferred, 1 mol of CO_2 is transferred as well (see Table 8). Thus, the H_2 local mass transfer profile is nearly 4 times larger than that of CO_2.

Fig. 12 shows the local profile obtained at steady state. The gaseous substrates (H_2 & CO_2) enter the column are transferred and consumed. The model predicts more than 95% CO_2 removal and conversion into CH_4. The outlet CH_4 fraction reaches 95% with a flow rate of 123 Nm³/h which corresponds closely to the output reported at the full industrial scale (Table 7) and validate thus globally the 1D comprehensive model in a real installation. This result was obtained by setting the initial bubble diameter to 2 mm and using the Higbie correlation for k_L. Some other combination might work equally well. The satisfactory comparison to the
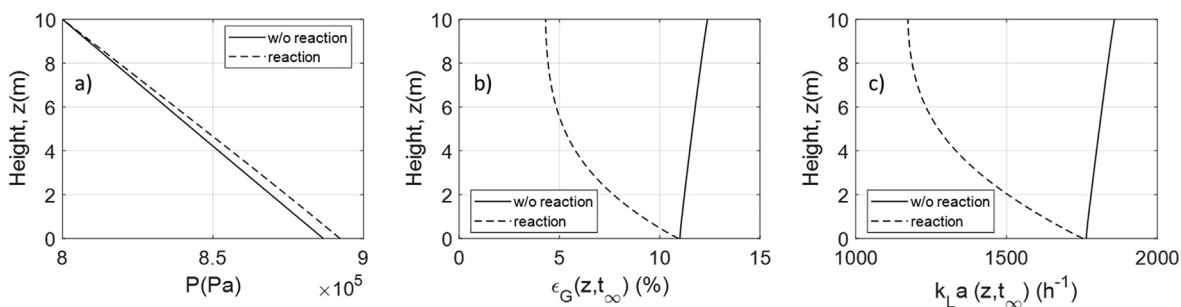
Fig. 10. Steady-state hydrodynamic variables spatial profile. The legend **w/o reaction** and **reaction** refer to the case without reaction and with reaction respectively.
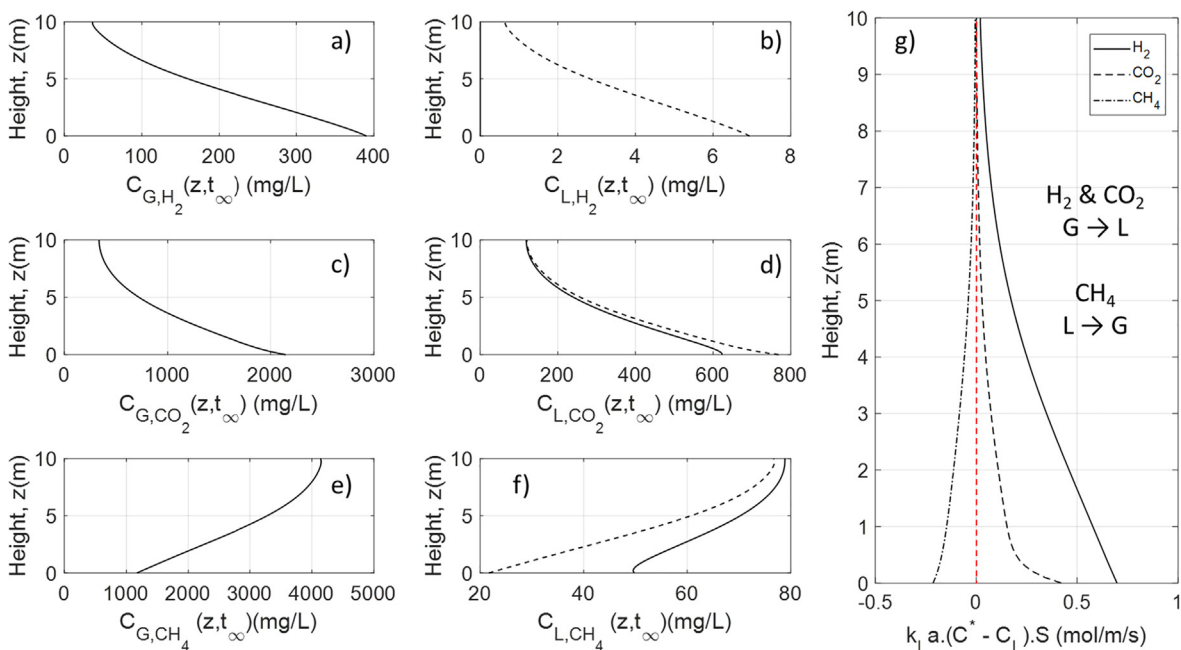

Fig. 11. Steady-state concentration spatial profile. Graph legend for liquid and equilibrium concentration as follows: $-$ and $- -$ are for $C_{L,i}$ and C^* profile respectively.
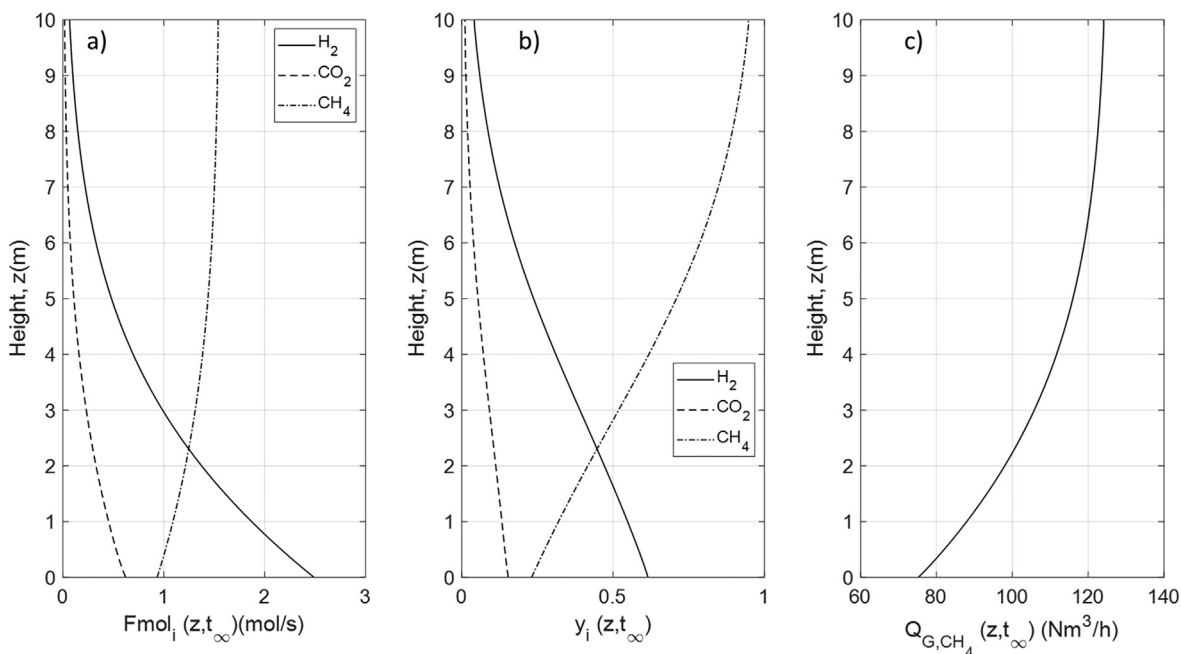

Fig. 12. Industrial scale biological methanation performance. (a) Gas phase local molar flux (b) gas phase molar fraction and (c) methane production.

Table 7

Model predicted results vs. reported values from the literature.

Outlet value	Reported data from (Electrochaea – Carbon and Energy storage, 2017; Forstmeier, n.d.)	This work
$Q_{G,CH4}$ (Nm³/h)	125	123
yCH_4 (%)	95–97	95

Table 9

Evaluation of H_2 biological demand and physical supply in Eq. (16) at three different time instants valued in mol/s.

Time	Total biological demand $S \cdot \int_0^z q_{H_2}^{max} \cdot \frac{C_{L,H_2}}{K_{H_2}+C_{L,H_2}} \cdot X \cdot dz$	Total physical supply $S \cdot \int_0^z max\left(\frac{k_L a_{H_2} C_{L,H_2}}{\varepsilon_L}, \frac{C_{L,H_2}}{\tau_m}\right) \cdot dz$
t = 400 s	2.30	2689
t = 19,900 s	6.41	376
t=t_∞	11.88	6.72

outlet concentration actually validates the integral value of $k_L a$ at the reactor scale as no concentration profile like in the work of Deckwer et al. in Section 3.2 are available for local validation at industrial scale.

From Table 8, it is observed that the H_2: CO_2 gaseous molar ratio of 4:1 imposed at the inlet corresponds to the ratio of the gas transferred (T_{H2}: T_{CO2}) at the steady state. This is due to the overall limiting process is originated from the H_2 mass transfer. Therefore, the CO_2 and CH_4 mass transfer are conditioned by the stoichiometry of the bioreaction, as stated in Eq. (13).

A strength of the proposed approach is to handle the transition from the biological regime to the physical regime. Indeed, in a bioreactor where substrates are provided in the gas phase only, biomass keeps growing until the gas–liquid mass transfer becomes the limiting phenomena as reported in Table 9. In order to illustrate this succession of events, the vertical profiles of local H_2 consumption rate φ_{H_2}, expressed either as the biological consumption rate or the physical supply of H_2 mass transfer rate, are plotted in Fig. 13 at different times.

At the beginning of the process around t = 400 s (Fig. 13a), H_2 is abundant in the reactor with very little biomass in it (initial concentration at 1 g/L, as shown in Fig. 14), the mass transfer is not limiting the overall reaction. It is observed that φ_{H_2} is equals to $q_{H_2}^{max}$ and the column operates in the biological regime. As the biomass concentration increases in the reactor, the demand for H_2 increases. At t = 19,900 s (Fig. 13b), this demand is fulfilled in the lower part of the column which still operates in the biological regime, but it is insufficient in the upper part where the actual specific uptake rate is limited by the local mass transfer. In the lower part, the gas phase is still rich in H_2 while H_2 is depleted in the gas phase in the upper part. A steady-state is reached when the H_2 mass transfer becomes the limiting step everywhere.

Fig. 14 depicts the evolution of biomass concentration until steady state. Dynamic simulation shows that the biomass reaches a concentration of 35 g/L at steady state. This value can be compared to an estimate based on the assumption that gas–liquid mass transfer is limiting the bioreaction everywhere in the reactor. Such a situation is actually taking place at steady state as shown in Fig. 13c (t = 59,900 s). This implies that the amount of hydrogen supplied is used for maintenance purposes only and the overall specific growth rate is null. Therefore, the steady state biomass concentration can be obtained from the solution of $R_X = Y_{X/H_2}(r_1 - r_3) = Y_{X/H_2} \cdot \left(\varphi_{H_2} - m\right) \cdot X = 0$. Using Eq. (16) in the regime of gas liquid mass transfer limitation, one gets $\langle \varepsilon_L X \rangle = \frac{\langle k_L a_{H_2} C_{L,H_2} \rangle}{m}$ which leads to a value of 35.8 g/L for the biomass concentration. This value is very close to the biomass concentra-

tion at steady state, suggesting that the model for biological reaction calculation is consistent and correctly implemented into the numerical simulation.

With the new formulation of substrate uptake rate as written in Eq. (16), it can be observed that:

i. This rate limiting-step formulation provides an elegant way to circumvent the numerical issues related to extremely low values for K_{H2}, which led Inkeri and co-workers to introduce artificial stabilizing function I_D and I_C in their model (see Eqs. (46) and (47) in (Inkeri et al., 2018)

ii. At low biomass concentration, the uptake rate is set by the biological capacity of the microorganisms and is almost constantly equal to $q_{H_2}^{max}$ since the value of K_{H2} is extremely low (5.6 $\mu mol \cdot L^{-1}$ as reported by Schill et al. (1999)

iii. As the biomass increases, the specific uptake rate will become limited by the gas–liquid mass transfer rate.

iv. Mass transfer limitation coincides with almost zero hydrogen concentration. However, when the hydrogen concentration is close to zero, the actual specific uptake rate is not zero (typically the case when the uptake rate is expressed in terms of concentration, such as Monod-type expression) but equals the maximum mass transfer rate per cell mass indicating that bioreactions are limited by the gas–liquid mass transfer rate. Thus, growth will still be possible.

v. According to Eqs. (15)–(19), growth will finally stop when $\varphi_{H_2} = m$. Thus, a constant biomass concentration will be reached when hydrogen uptake is limited by gas–liquid mass transfer and the amount of hydrogen is just sufficient to meet the cell's requirements for maintenance. From that point onward, we will observe that $k_L a_{H_2} \cdot C_{L,H_2}^* = m \cdot \varepsilon_L \cdot X$ and the other kinetic equations indicate that constant carbon dioxide consumption and methane production rates will be attained, both being proportional to $k_L a_{H_2} C_{L,H_2}^*$.

vi. (Markthaler et al., 2020) used a second order kinetics law to describe biological methanation. In accordance with (Schill et al., 1999) conclusions, these authors observed that the kinetic rate constant itself is of minor importance since biological reactions rates are, in the end, controlled by the interfacial mass transfer rate. Here, we proposed a more meaningful formulation for the biokinetics model capable to capture the competitive balance between biological demand and mass transfer supply.

5. Conclusion and outlook

It is well-known in the literature that the modeling of biological processes requires a two-way coupling approach for mass transfer and hydrodynamics. But in practice, either very few models have done so or the two-way coupling has not been implemented delicately and discussed in details (Inkeri et al., 2018; de Medeiros et al., 2020; Chen et al., 2016, 2015). Therefore, a new 1D gas–liquid multispecies mass transfer and spatio-temporal model is established to model the biological methanation process in bubble
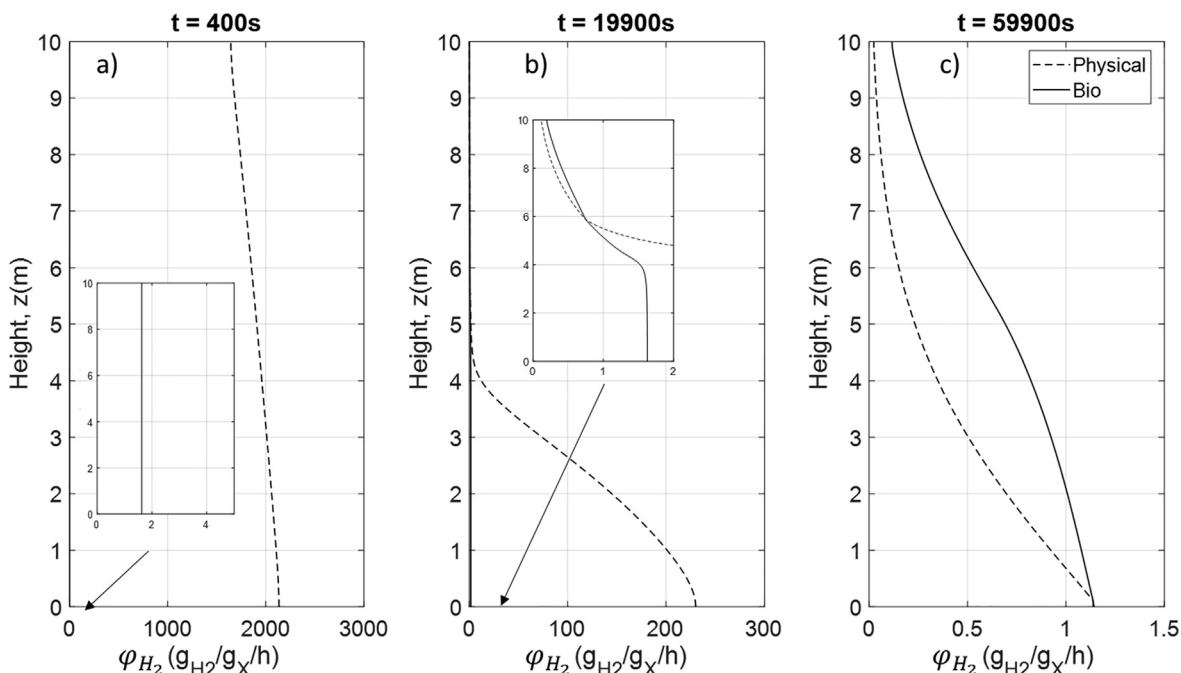
Table 8

H_2, CO_2 & CH_4 local mass transfer flux.

Species, i	H_2	CO_2	CH_4
$F_{i,in}$ (mol/s)	2.48	0.62	0.93
T_i (t = t_∞) (mol/s)	2.43	0.61	−0.61
Yield = T/F_{in} (%)	98	98	–

Fig. 13. Revealing the regime transition: biological consumption rate and specific H_2 mass transfer rate as presented in Eq. (16).
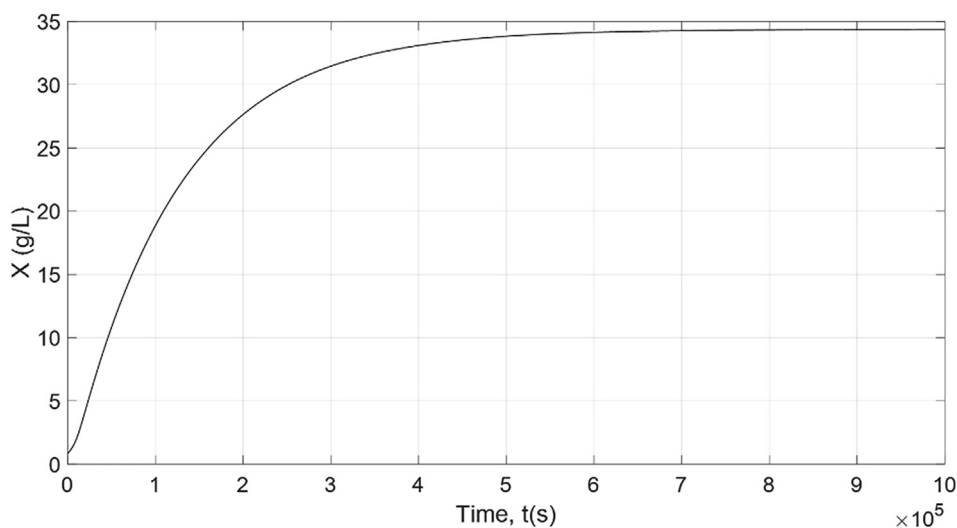

Fig. 14. Temporal evolution of biomass weight in g per L of total reactor volume.

columns. The model developed considers the 1D two phase flow, whereby the mass transfer and bioreaction rate impact the hydrodynamics local profile, in return the hydrodynamics quantifies the interphase mass transfer rate and the bioreaction rate. The two-way coupled 1D model developed here is in good agreement with previous experimental and literature data. The knowledge of bubble size is crucial but no further fitting parameters are needed to obtain good prediction in the very case where bioreaction rates are controlled by gas–liquid mass transfer. For the bubbly flow hydrodynamics, the model is validated using our experimental transient gas holdup measurements and literature data. A satisfactory predication of the local gas holdup profile and mass transfer, behavior was shown in comparison to the results of Deckwer et al. (1978) and Hissanaga et al. (2020). Strong variation of local gas holdup due to high interphase CO_2 mass transfer flux are correctly addressed. Local mass transfer flux of each species i are cap-

tured precisely by the model which is crucial to simulate the biological reaction. The effect of hydrostatic pressure and column height was studied and it is found that non-linearities and heterogeneities prevails in tall bubble column. Due to differences in the gaseous substrates' solubility (H_2 & CO_2), the local concentrations and therefore the local mass transfer fluxes of each species vary along the height of the column. As a result, the molar ratio imposed at the inlet is not conserved, signifying that the mass transfer rate changes according to the species. Lastly, the model has been extended to an industrial-scale biological methanation plant. In this type of bioprocess, where the substrates are fed through the gaseous phase only the performances are limited by the slowest mass transfer rate (H_2 for biomethanation). Contrary to (Inkeri et al., 2018) and (Markthaler et al., 2020) work, the new proposed biological uptake rate has a more physical significance. As pointed out by Schill et al., the description of the kinetics of growth should

be written as the uptake kinetics of the limiting substrate that controls the whole bioreaction process (Schill et al., 1999). In this work, we proposed to describe the substrate uptake rate by using the minimum between the biological Monod-type uptake rate and the locally available specific H_2 supply. The latter is expressed as the maximum between the specific mass transfer rate (when the dissolved H_2 in the environment is depleted) and the specific local concentration renewed by the micromixing. This signifies the limiting factor can either comes from the biological origin or the physical origin. The results of this formulation have been demonstrated in the simulation of industrial-scale biological methanation as the results is closely matched the reported values. In future work, this comprehensive 1D model will be used to study scale-up and addresses two-way coupling issues faced in the industrial biological bubble column. The 1D model with the novel bioreaction closure model will also be used as a baseline reference for multispecies two-phase flow in a more complex geometry whereby two-fluid CFD model could be extended to study multispecies two-way coupling with bioreaction.

CRediT authorship contribution statement

Vincent Ngu: Methodology, Conceptualization, Writing – original draft, Software, Data curation, Validation. **Jérôme Morchain:** Supervision, Methodology, Conceptualization, Writing – review & editing, Software. **Arnaud Cockx:** Supervision, Methodology, Conceptualization, Writing – review & editing.

Declaration of Competing Interest

The authors declare that they have no known competing financial interests or personal relationships that could have appeared to influence the work reported in this paper.

Acknowledgement

Appendix A

Drag model

Tomiyama et al. (1998)
$$C_D = \max \left\{ \min \left[\frac{24}{Re_b} \left(1 + 0.15 Re_b^{0.687} \right), \frac{72}{Re_b} \right], \frac{8}{3} \frac{Eo}{(4+Eo)} \right\} \quad (A.1)$$

Mei et al. (1994)

$$C_D = \frac{16}{Re_b} \left(1 + \frac{Re_b}{8 + 0.5(Re_b + 3.315 Re_b^{0.5})} \right) \quad (A.2)$$

Dijkhuizen et al. (2010)

$$C_D = \sqrt{C_D(Re_b)^2 + C_D(Eo)^2}$$
$$C_D(Re_b) = C_D \text{ from Eq. (A.2)}$$
$$C_D(Eo) = \frac{4.Eo}{9.5 + Eo} \quad (A.3)$$

Appendix B

Details of iterative resolution of system (20)

The algorithm is a successive substitution procedure. Starting from the known local molar fluxes ($\phi_{G,i}$, $\phi_{L,i}$) and the local gas holdup (ε_G), the local pressure profile (P), the local gas holdup (ε_G) as well as $C_{G,i}$ and $C_{L,i}$ are updated before the next timestep is taken.

The following procedure is used at the beginning of each timestep.

Step 1. $\phi_{G,i} \leftarrow \phi_{G,i}(t)$ and $\varepsilon_G \leftarrow \varepsilon_G(t)$

Step 2. $C_{G,i} \leftarrow \frac{\phi_{G,i}}{\varepsilon_G}$

Step 3. Update P from ε_G using equation (10)

Step 4. Update the local gas fraction $\varepsilon_G \leftarrow \frac{\sum \phi_{G,i}/M_i}{P} RT$

Step 5. Repeat Step 2 to 4 until the difference between two iterations falls below a given tolerance

Step 6. Update the liquid phase concentrations $C_{L,i} = \phi_{L,i}/(1 - \varepsilon_G)$

The updated $C_{G,i}$, $C_{L,i}$ and ε_G are used in the right-hand side of Eqs. (1) and (2) to compute the time derivatives.

Appendix C

Bubble geometrical characteristics

With a total of 1000 images taken, the statistical convergence was reached as a significant number of bubbles were detected. Example of bubble images provided from Cam1 centered in the cylindrical bubble column are presented in Fig. C.1. The acquisition window of 26×26 mm^2 is small in comparison to the column diameter of 150 mm. It is noticeable that the bubble number and bubble sizes increase with increasing flow rate. The equivalent diameter calculated were represented in the form of histogram with a bin of 0.2 mm, as shown in Fig. C.2. The bubble size detected
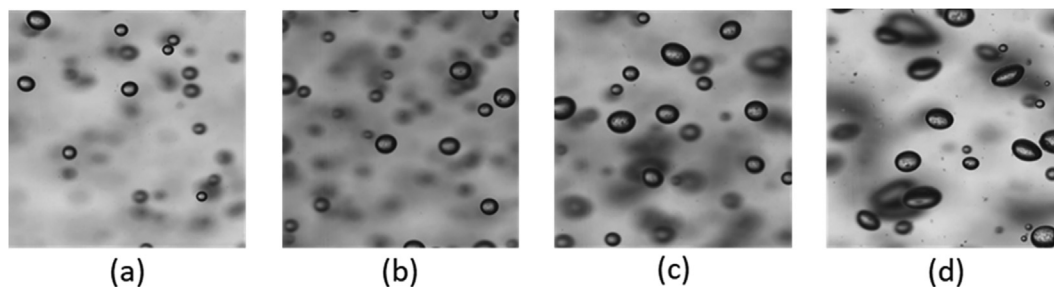

Fig. C.1. Raw images (a)–(d) refers to j_G = 0.039 cm/s, 0.078 cm/s, 0.116 cm/s and 0.156 cm/s respectively.
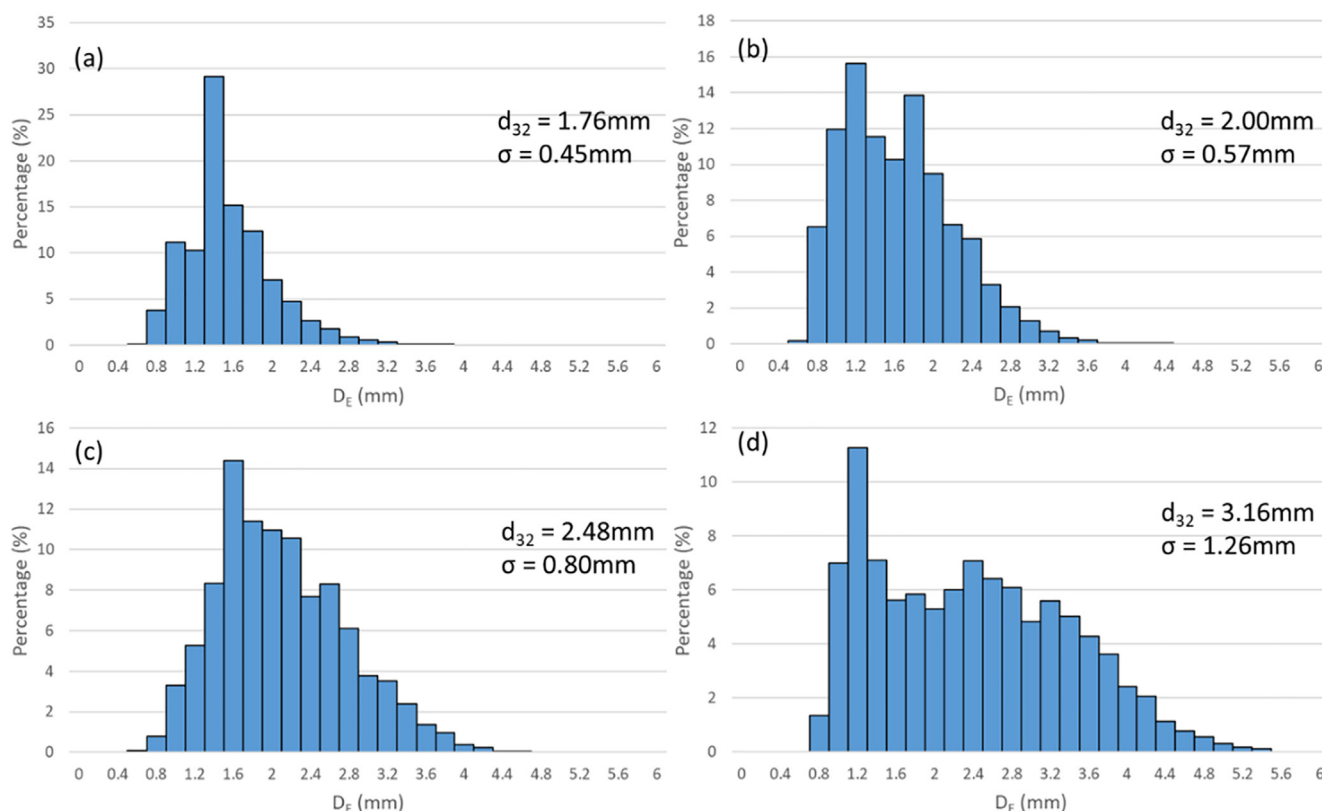
Fig. C.2. Histogram of bubble size distribution (a)–(d) refers to j_G = 0.039 cm/s, 0.078 cm/s, 0.116 cm/s, and 0.156 cm/s respectively.

and its standard deviation increased with the flow rate. The bubble size distribution was mostly mono-dispersed which is almost the case in homogeneous bubbly flow regime. This also validates the choice of using single-bubble class for our model by using the d_{32} of each case.

Appendix D

Statistical average of ΔH

Fig. D.1 plots the cumulative average of ΔH versus the image number. The curve is not constant which indicates the fluctuating nature of the free surface, but they eventually reach a stable value with increasing image number. As observed, the difference between the cumulative statistical average of ΔH and the ΔH taken at the last image upon the first bubble arrival is insignificant. Here, the ΔH obtained was 2.91 vs 2.98 mm. This result in a $\langle \varepsilon_{G,exp} \rangle$ of 0.277% vs 0.283%, a negligible relative difference of 5%.
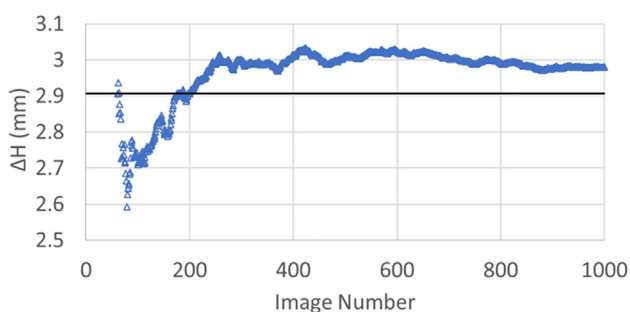

Fig. D.1. Continuous line is ΔH taken at the last image vs Δ symbol the cumulative average of ΔH.

References

Bardin-Monnier, N., Guiraud, P., Gourdon, C., 2003. Lagrangian simulations contribution to the knowledge of discs and doughnuts pulsed solvent extraction columns hydrodynamics. Chem. Eng. Process. Process Intensif. 42 (7), 503–516. https://doi.org/10.1016/S0255-2701(02)00072-7.

Bassani, I., Kougias, P.G., Angelidaki, I., 2016. In-situ biogas upgrading in thermophilic granular UASB reactor: key factors affecting the hydrogen mass transfer rate. Bioresour. Technol. 221, 485–491. https://doi.org/10.1016/j.biortech.2016.09.083.

Besagni, G., Inzoli, F., 2016. Comprehensive experimental investigation of counter-current bubble column hydrodynamics: Holdup, flow regime transition, bubble size distributions and local flow properties. Chem. Eng. Sci. 146, 259–290. https://doi.org/10.1016/j.ces.2016.02.043.

Besagni, G., Inzoli, F., Ziegenhein, T., Lucas, D., 2019. The pseudo-homogeneous flow regime in large-scale bubble columns: experimental benchmark and computational fluid dynamics modeling. Petroleum 5, 141–160. https://doi.org/10.1016/j.petlm.2017.12.004.

Chen, J., Brooks, C.S., 2021. Experiments and CFD simulation of mass transfer and hydrodynamics in a cylindrical bubble column. Chem. Eng. Sci. 234,. https://doi.org/10.1016/j.ces.2020.116435 116435.

Chen, J., Gomez, J.A., Höffner, K., Barton, P.I., Henson, M.A., 2015. Metabolic modeling of synthesis gas fermentation in bubble column reactors. Biotechnol. Biofuels 8, 89. https://doi.org/10.1186/s13068-015-0272-5.

Chen, J., Gomez, J.A., Höffner, K., Phalak, P., Barton, P.I., Henson, M.A., 2016. Spatiotemporal modeling of microbial metabolism. BMC Syst. Biol. 10, 21. https://doi.org/10.1186/s12918-016-0259-2.

Chen, J., Daniell, J., Griffin, D., Li, X., Henson, M.A., 2018. Experimental testing of a spatiotemporal metabolic model for carbon monoxide fermentation with Clostridium autoethanogenum. Biochem. Eng. J. 129, 64–73. https://doi.org/10.1016/j.bej.2017.10.018.

Darmana, D., Henket, R.L.B., Deen, N.G., Kuipers, J.A.M., 2007. Detailed modelling of hydrodynamics, mass transfer and chemical reactions in a bubble column using a discrete bubble model: Chemisorption of CO2 into NaOH solution, numerical and experimental study. Chem. Eng. Sci. 62, 2556.

de Medeiros, E.M., Noorman, H., Maciel Filho, R., Posada, J.A., 2020. Production of ethanol fuel via syngas fermentation: Optimization of economic performance and energy efficiency. Chem. Eng. Sci.: X 5,. https://doi.org/10.1016/j.cesx.2020.100056 100056.

Deckwer, W.-D., Adler, I., Zaidi, A., 1978. A comprehensive study on CO2-interphase mass transfer in vertical cocurrent and countercurrent gas-liquid flow. Can. J. Chem. Eng. 56 (1), 43–55.

Deckwer, W.-D., Burckhart, R., Zoll, G., 1974. Mixing and mass transfer in tall bubble columns. Chem. Eng. Sci. 29 (11), 2177–2188. https://doi.org/10.1016/0009-2509(74)80025-4.

Deckwer, W.-D., Schumpe, A., 1993. Improved tools for bubble column reactor design and scale-up. Chem. Eng. Sci. 48 (5), 889–911. https://doi.org/10.1016/0009-2509(93)80328-N.

Di Giuliano, A., Pellegrino, E., 2019. Numerical integration strategies of PFR dynamic models with axial dispersion and variable superficial velocity: the case of CO2 capture by a solid sorbent. Heliyon 5,. https://doi.org/10.1016/j.heliyon.2019.e02040 e02040.

Dijkhuizen, W., Roghair, I., Van Sint Annaland, M., Kuipers, J.A.M., 2010. DNS of gas bubbles behaviour using an improved 3D front tracking model—Drag force on isolated bubbles and comparison with experiments. Chem. Eng. Sci. 65 (4), 1415–1426. https://doi.org/10.1016/j.ces.2009.10.021.

Electrochaea – Carbon and Energy storage, 2017. https://www.europeanbiogas.eu/wp-content/uploads/2017/09/7.-Electrochaea_EBA_Sept2017.pdf.

Electrochaea GmbH, n.d. http://www.electrochaea.com/ (accessed March 8, 2021).

Forstmeier, D.M., n.d. Biological methanation for grid scale carbon & energy storage. Vol. 17.

Giovannettone, J.P., Gulliver, J.S., 2008. Gas transfer and liquid dispersion inside a deep airlift reactor. AIChE J. 54 (4), 850–861. https://doi.org/10.1002/aic.11449.

Giovannettone, J.P., Tsai, E., Gulliver, J.S., 2009. Gas void ratio and bubble diameter inside a deep airlift reactor. Chem. Eng. J. 149 (1-3), 301–310. https://doi.org/10.1016/j.cej.2008.11.024.

Heijnen, J.J., Van't Riet, K., 1984. Mass transfer, mixing and heat transfer phenomena in low viscosity bubble column reactors. Chem. Eng. J. 28, B21–B42. https://doi.org/10.1016/0300-9467(84)85025-X.

Higbie, R., 1935. The Rate of Absorption of a Pure Gas into a Still Liquid during Short Periods of Exposure. Trans. AIChE. 31, 365–389.

Hissanaga, A.M., Padoin, N., Paladino, E.E., 2020. Mass transfer modeling and simulation of a transient homogeneous bubbly flow in a bubble column. Chem. Eng. Sci. 218,. https://doi.org/10.1016/j.ces.2020.115531 115531.

Hlawitschka, M.W., Kováts, P., Zähringer, K., Bart, H.-J., 2017. Simulation and experimental validation of reactive bubble column reactors. Chem. Eng. Sci. 170, 306–319. https://doi.org/10.1016/j.ces.2016.12.053.

Inkeri, E., Tynjälä, T., Laari, A., Hyppänen, T., 2018. Dynamic one-dimensional model for biological methanation in a stirred tank reactor. Appl. Energy 209, 95–107. https://doi.org/10.1016/j.apenergy.2017.10.073.

Inkeri, E., Tynjälä, T., 2020. Modeling of CO2 Capture with Water Bubble Column Reactor. Energies 13, 5793. https://doi.org/10.3390/en13215793.

Inoue, K., 1973. Method of determining the coefficient of longitudinal mixing for the continuous phase under conditions of a non flow-through system in high rate extractors. Theoreticheskie Osnovy Khimicheskoi Tekhnologii, 550–556.

Kováts, P., Thévenin, D., Zähringer, K., 2020. Influence of viscosity and surface tension on bubble dynamics and mass transfer in a model bubble column. Int. J. Multiph. Flow 123,. https://doi.org/10.1016/j.ijmultiphaseflow.2019.103174 103174.

Laupsien, D., Le Men, C., Cockx, A., Liné, A., 2019. Image processing for bubble morphology characteristics in diluted bubble swarms. Phys. Fluids 31,. https://doi.org/10.1063/1.5088945 053306.

Lecker, B., Illi, L., Lemmer, A., Oechsner, H., 2017. Biological hydrogen methanation – A review. Bioresour. Technol. 245, 1220–1228. https://doi.org/10.1016/j.biortech.2017.08.176.

Li, X., Griffin, D., Li, X., Henson, M.A., 2019. Incorporating hydrodynamics into spatiotemporal metabolic models of bubble column gas fermentation. Biotechnol. Bioeng. 116 (1), 28–40. https://doi.org/10.1002/bit.26848.

Linkès, M., 2012. Numerical Simulation and modelling of substrate assimilation by microorganisms in a turbulent flow, phd. http://ethesis.inp-toulouse.fr/archive/00002128/ (accessed May 25, 2021).

Markthaler, S., Plankenbühler, T., Weidlich, T., Neubert, M., Karl, J., 2020. Numerical simulation of trickle bed reactors for biological methanation. Chem. Eng. Sci. 226,. https://doi.org/10.1016/j.ces.2020.115847 115847.

Mei, R., Klausner, J.F., Lawrence, C.J., 1994. A note on the history force on a spherical bubble at finite Reynolds number. Phys. Fluids 6, 418–420. https://doi.org/10.1063/1.868039.

Morchain, J., Gabelle, J.-C., Cockx, A., 2014. A coupled population balance model and CFD approach for the simulation of mixing issues in lab-scale and industrial bioreactors. AIChE 60 (1), 27–40. https://doi.org/10.1002/aic.14238.

Morchain, J., Pigou, M., Lebaz, N., 2017. A population balance model for bioreactors combining interdivision time distributions and micromixing concepts. Biochem. Eng. J. 126, 135–145. https://doi.org/10.1016/j.bej.2016.09.005.

Nauha, E.K., Alopaeus, V., 2015. Modeling outdoors algal cultivation with compartmental approach. Chem. Eng. J. 259, 945–960. https://doi.org/10.1016/j.cej.2014.08.073.

Pigou, M., Morchain, J., 2015. Investigating the interactions between physical and biological heterogeneities in bioreactors using compartment, population balance and metabolic models. Chem. Eng. Sci. 126, 267–282. https://doi.org/10.1016/j.ces.2014.11.035.

Pigou, M., 2018. Modélisation du comportement cinétique, des phénomènes de mélange et de transfert locaux, et des effets d'hétérogénéité de population dans les fermenteurs industriels, These de doctorat, Toulouse, INSA. http://www.theses.fr/2018ISAT0038 (accessed June 9, 2021).

Rafrafi, Y., Laguillaumie, L., Dumas, C., 2020. Biological Methanation of H2 and CO2 with Mixed Cultures: Current Advances, Hurdles and Challenges. Waste Biomass Valor. https://doi.org/10.1007/s12649-020-01283-z.

Rusmanis, D., O'Shea, R., Wall, D.M., Murphy, J.D., 2019. Biological hydrogen methanation systems – an overview of design and efficiency. Bioengineered 10 (1), 604–634. https://doi.org/10.1080/21655979.2019.1684607.

Rzehak, R., Krepper, E., 2016. Euler-Euler simulation of mass-transfer in bubbly flows. Chem. Eng. Sci. 155, 459–468. https://doi.org/10.1016/j.ces.2016.08.036.

Sander, R., 2015. Compilation of Henry's law constants (version 4.0) for water as solvent. Atmos. Chem. Phys. 15 (8), 4399–4981. https://doi.org/10.5194/acp-15-4399-2015.

Sasaki, S., Uchida, K., Hayashi, K., Tomiyama, A., 2017. Effects of column diameter and liquid height on gas holdup in air-water bubble columns. Exp. Therm Fluid Sci. 82, 359–366. https://doi.org/10.1016/j.expthermflusci.2016.11.032.

Schill, N.A., Liu, J.-S., von Stockar, U., 1999. Thermodynamic analysis of growth of Methanobacterium thermoautotrophicum. Biotechnol. Bioeng. 64, 74–81. https://doi.org/10.1002/(SICI)1097-0290(19990705)64:1<74::AID-BIT8>3.0.CO;2-3.

Shah, Y.T., Kelkar, B.G., Godbole, S.P., Deckwer, W.-D., 1982. Design parameters estimations for bubble column reactors. AIChE J. 28 (3), 353–379. https://doi.org/10.1002/aic.690280302.

Siebler, F., Lapin, A., Takors, R., 2020. Synergistically applying 1-D modeling and CFD for designing industrial scale bubble column syngas bioreactors. Eng. Life Sci. 20 (7), 239–251. https://doi.org/10.1002/elsc.201900132.

Sveinbjörnsson, D., Münster, E., 2017. Gas conditioning and grid operation: Upgrading of Biogas to Biomethane with the Addition of Hydrogen from Electrolysis. https://futuregas.dk/wp-content/uploads/2018/06/FutureGas-WP1-Deliverable-1.1.1.-Technologies-and-status-of-methanation-of-biogas-2017_Final.pdf.

Tomiyama, A., Kataoka, I., Zun, I., Sakaguchi, T., 1998. Drag Coefficients of Single Bubbles under Normal and Micro Gravity Conditions. JSME Int. J. Ser. B 41 (2), 472–479. https://doi.org/10.1299/jsmeb.41.472.

Versteeg, G.F., Van Swaaij, W.P.M., 1988. Solubility and diffusivity of acid gases (carbon dioxide, nitrous oxide) in aqueous alkanolamine solutions. J. Chem. Eng. Data 33 (1), 29–34. https://doi.org/10.1021/je00051a011.

Wachi, S., Nojima, Y., 1990. Gas-phase dispersion in bubble columns. Chem. Eng. Sci. 45 (4), 901–905. https://doi.org/10.1016/0009-2509(90)85012-3.